Correction Formulas for the Mølmer-Sørensen Gate

Dissertation zur Erlangung des Grades der Doktorin der Naturwissenschaften der Naturwissenschaftlich-Technischen Fakultät der Universität des Saarlandes

von
Susanna Kirchhoff

Saarbrücken

2025

Tag des Kolloquiums:	02.12.2025
Dekan:	Prof. Dr.-Ing. Dirk Bähre
Berichterstattung:	Prof. Dr. Frank Wilhelm-Mauch Prof. Dr. Tommaso Calarco
Vorsitz:	Prof. Dr. Giovanna Morigi
Akad. Mitglied:	Dr. habil. Philipp Hövel

Dein Weltbild, Zwerg, wie du auch sinnst, bleibt ein Phantom, ein Hirngespinst.

Mascha Kaléko

Acknowledgements

The past few years have been tough. The pandemic, the transition of our group from Saarbrücken to becoming an institute in Jülich, and I have complicated my way towards a PhD. All the more, I would like to thank those who supported me. First, I wish to express my thanks to Frank Wilhelm-Mauch for offering me the opportunity for the PhD and for his persistent support, while giving me a lot of freedom. Then, I would like to thank Felix Motzoi for his motivation and close supervision, which led to the successful publication of our paper. Also, I want to acknowledge the support from my peers in the group/institute. Specifically, thanks to the younger generation for creating a new group spirit, the "Writers' Club" for systematic support, as well as thanks to my teaching companions Nico, Andrii, and Raphi for many interesting discussions and fun. A big thank-you goes to my duck friends (and acquaintances) for reliable weekly meetings and always having an open ear. Last but not least, I am grateful for the emotional support from my friends, family and Christoph.

Abstract

The Mølmer-Sørensen gate is a common entangling quantum gate for trapped-ion platforms that has reached fidelities around 99.7 % in experiment. Those fidelities could not be fully explained theoretically. We explain in detail that the error is inherent to the construction of the Mølmer-Sørensen gate, and we show, analytically and numerically, that the errors can be partially compensated by adjusting the drive amplitude, and with pulse shaping of the drive amplitude.

To calculate the fidelity of the gate, it is useful to find the time evolution operator of the system by calculation of an effective Hamiltonian using the Magnus expansion. Before calculation of the Magnus expansion, the Hamiltonian can be simplified by expanding it into a Taylor series in the Lamb-Dicke factor and cutting off higher order terms. In this case, the Magnus expansion yields as exact result the first nonvanishing order.

In our work, we calculate the Magnus expansion without cutting off the Taylor series before and find that in this case additional terms appear in the Magnus expansion. Those terms can change the gate infidelity by orders of magnitudes and thus are significant contributions that should not be neglected by default. We demonstrate, how adjusting the drive amplitude can partially suppress those additional terms. Furthermore, we present the results for shaped pulses as well, showing that a smooth drive pulse, specifically $\sin^2$, can reduce the additional errors.

Zusammenfassung

Das Mølmer-Sørensen-Gatter (MSG) wird häufig zur Erzeugung von verschränkten Zuständen auf Ionenplattformen genutzt und erreicht experimentell eine Fidelität von 99.7 %.

Quantenmechanisch wird das MSG mit einem zeitabhängigen Hamiltonoperator (HO) für die Wechselwirkung zwischen den Ionen und ihren elektronischen Zuständen unter Einwirkung von Laserpulsen beschrieben. Daraus kann man mit der Magnusreihe einen effektiven zeitunabhängigen HO berechnen, dessen Dynamik denselben Endzustand ergibt wie der zeitabhängige HO.

Um den effektiven HO berechnen zu können, wird der zeitabhängige HO in eine Taylorreihe im Lamb-Dicke-Faktor entwickelt. Ist dieser klein, werden üblicherweise die höheren Ordnungen der Taylorreihe vernachlässigt. In diesem Fall beschränkt sich der effektive HO auf die niedrigste nichtverschwindenden Ordnung der Magnusreihe, die dem HO eines verschränkenden Gatter entspricht.

In dieser Arbeit wird der effektive HO berechnet, ohne zuvor Terme der Taylorreihe des zeitabhängigen HO zu vernachlässigen und aufgezeigt, dass zumindest die beiden nächsthöheren Terme der Magnusreihe bei der Bestimmung des effektiven HO berücksichtigt werden sollten. Die Ergebnisse werden analytisch hergeleitet und numerisch untermauert, womit einige Limitierungen der Fidelität des MSG erklärt werden können. Zudem demonstrieren wir, ebenfalls analytisch und numerisch, dass mithilfe einer zeitabhängigen Einhüllenden der Amplitude des Laserpulses die Fidelität deutlich verbessert werden kann.

List of Publications

Published

- Susanna Kirchhoff, Frank K. Wilhelm, and Felix Motzoi. "Correction Formulas for the Mølmer-Sørensen Gate Under Strong Driving". Version 2. In: *PRX Quantum* 6.1 (Feb. 12, 2025), p. 010328. DOI: 10.1103/PRXQuantum.6.010328

Other

- Susanna Kirchhoff, Torsten Keßler, Per J. Liebermann, Elie Assémat, Shai Machnes, Felix Motzoi, and Frank K. Wilhelm. "Optimized Cross-Resonance Gate for Coupled Transmon Systems". In: *Physical Review A* 97.4 (Apr. 30, 2018), p. 042348. DOI: 10.1103/PhysRevA.97.042348
- Frank K. Wilhelm, Susanna Kirchhoff, Shai Machnes, Nicolas Wittler, and Dominique Sugny. "An Introduction into Optimal Control for Quantum Technologies". Mar. 23, 2020. DOI: 10.48550/arXiv.2003.10132. Prepublished
- Frank K. Wilhelm, Rainer Steinwandt, Daniel Zeuch, Paul Lageyre, and Susanna Kirchhoff. *Status of quantum computer development*. Federal Office for Information Security, Jan. 2, 2025. URL: https://www.bsi.bund.de/SharedDocs/Downloads/DE/BSI/Publikationen/Studien/Quantencomputer/Entwicklungstand_QC_V_2_1.pdf?__blob=publicationFile&v=3

Contents

List of Figures and Tables

Chapter 1.

Introduction

We live in times of the quantum hype [Bog+24; Con17]. There is an increasingly growing community working towards quantum advantage [Sac+24; McG+24; Aru+19; Ped+19; Mad+22]. But why is it not there yet? The answer lies in the nature of quantum computing. Classical computers work with bits that are either 1 or 0, while quantum bits, so called *qubits*, can additionally be in a *superposition* of both states. Furthermore, they can be *entangled* with another qubit or quantum system. Entanglement of two systems means that only the global state of the total system can be described, while the state of each subsystem is not well-defined.

These quantum properties are very sensitive to coupling with another system. Since couplings cannot be avoided—think of readout and control—quantum computing is intrinsically sensitive to types of errors that do only rarely or never occur—or are not even defined—in classical computing.

Fortunately, most of these errors can be corrected, as long as they are not correlated. While classical error correction algorithms would destroy the quantumness of the system, there exist advanced quantum error correction algorithm schemes, like for example the surface code [RH07; Fow+12]. In these algorithms, multiple physical qubits are connected to form a *logical qubit*. According to the threshold theorem [AB96; AB99], it is theoretically (and practically [Goo+25]) possible to achieve lower error rates in the logical qubits than in the physical qubits, provided that the physical error remains below a certain threshold value. The exact value of the threshold depends on the applied error correction code and the underlying error model. For instance, for the surface code the threshold

infidelity is approximately 0.75 % [RH07].

Errors accumulate during computation if the error in the physical qubits exceeds the threshold, making results unreliable. By contrast, the total error decreases if physical errors remain below the threshold and consequently, small error rates in the physical qubits are essential for successful quantum computing.

However, creating qubit gates with high fidelity can be a challenging task. While imperfections in the physical apparatus can make precise gate control difficult, another significant issue is the inadequate understanding of the system which needs to be controlled. Specifically, a drive pulse may lead to over- or under-rotations of a gate if parameters and drive method are not optimal. The reason for the non-optimal driving can be that the drive amplitude cannot be controlled exactly, but also that the drive mechanism does not work as predicted by the theory.

Clearly, a precise model of the system is crucial for useful implementations of theoretical constructions in experiments. For example, consider a qubit, that is, an effective two-level system. Often, a real quantum system possesses more than two accessible states, with the two qubit levels just being the most probable ones. A more nuanced understanding of the system, taking more levels into account, can provide valuable insight into phenomena such as population leakage, allowing to suppress leakage appropriately. In this context, the importance of precise models that can predict exactly where specific errors come from and how to correct them cannot be overstated.

In this dissertation, we will investigate inherent errors of an entangling gate for trapped ion qubits, the Mølmer-Sørensen gate. These can contribute significantly to the fidelity of the gate, hence an error budget that takes those errors into account is of great value.

In Section 1.1, we explain the basics of quantum computing, and in Section 1.2, we introduce trapped ions as a platform for quantum computing. In Section 2.1, we present the Hamiltonian for the Mølmer-Sørensen gate and discuss approximations on this Hamiltonian as well as standard methods for calculation of the time-development operator, among others the technique of the effective Hamiltonian. We derive in Section 2.2 resonance conditions for the effective Hamilto-

nian of the system. In Section 2.3, we provide analytical expression for terms of the effective Hamiltonian, for square drive pulses, and discuss suitable measures for the fidelity. Furthermore, we numerically evaluate the fidelity to examine the impact of the additional error terms. Moreover, we show, again analytically and numerically, in Section 2.4 that shaping the drive amplitude can reduce the fidelity. We finally summarize in Chapter 3 and give an outlook.

1.1. Gate-based quantum computing

The term "quantum computing" comprises, inter alia, quantum simulation [GAN14], adiabatic quantum computing [AL18], and gate-based quantum computing [NC10]. Quantum simulation uses a quantum system to simulate another quantum system, in adiabatic quantum computing, the solution of a problem is encoded in the ground state of a complex system, and gate-based quantum computing is similar to classical computing, except that different gate sets and algorithms are used.

Only recently, fault-tolerant quantum computing was demonstrated experimentally, yet only for quantum memory [Goo+25]. However, current leading experiments for gate-based quantum computing accomplish qubit numbers of the order of 10 to 100 [Goo+25; Pae+24; Bra+24], whereas with current knowledge around a million qubits are needed for practical applications like factorization of a 2048-bit number [Gid25]. John Preskill [Pre18] has coined the term *NISQ* (noisy intermediate scale quantum) era to describe this intermediate state in which prototypes for quantum computers exists, while quantum computing still misses the milestones that are needed for practical applications.

1.1.1. Qubits and gate operations

The state of a qubit is mathematically defined by a vector $\psi = (\alpha \quad \beta)^T$, where $\alpha, \beta \in \mathbb{C}$. We use from now on Dirac's Bra-Ket notation and write

$$|\psi\rangle = \alpha\,|0\rangle + \beta\,|1\rangle\,. \tag{1.1}$$

We see that the state $|\psi\rangle$ is in a superposition of the orthonormal basis states, which we call $|0\rangle$ and $|1\rangle$ and define to be the eigenstates of the Pauli operator $\hat{\sigma}_z$. The squared inner product between two states $|\langle\varphi|\psi\rangle|^2$ represents the probability of measuring $|\varphi\rangle$ when the system is in state $|\psi\rangle$. So, when measuring the qubit in the basis $\{|0\rangle, |1\rangle\}$, the outcome is $|0\rangle$ with probability $|\alpha|^2$ and $|1\rangle$ with probability $|\beta|^2$.

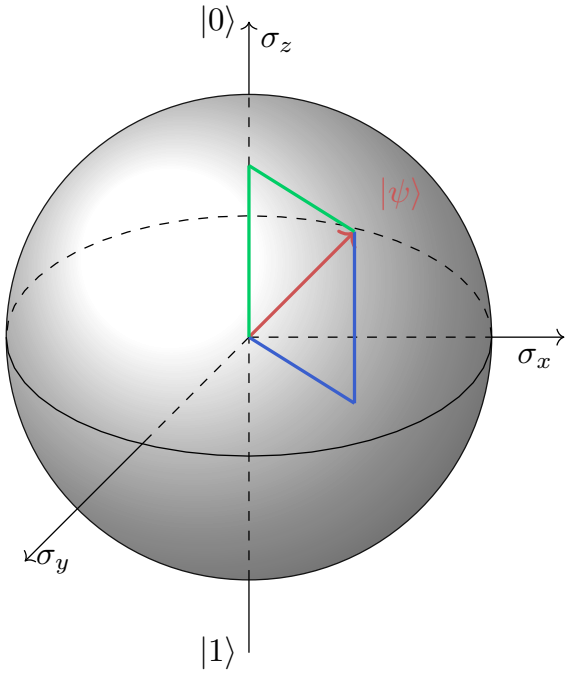

Figure 1.1.: The Bloch sphere can help to visualize the state of a qubit. Because the state of a qubit in a closed system is normalized $\langle\psi|\psi\rangle = 1$, the vector $|\psi\rangle$ always lies on a sphere with radius 1. The projection of a state $|\psi\rangle$ on the x, y, z-axis denotes the expectation value of the Pauli-x, y, z matrix $\langle\psi|\hat{\sigma}_{x,y,z}|\psi\rangle$ when measuring in the ψ-basis.

In a closed system, the probability of measuring a state in its eigenbasis equals to 1, so $\langle\psi|\psi\rangle = 1 = |a|^2 + |b|^2$. A general way to express a and b under this condition, omitting a global phase, is

$$|\psi\rangle = \cos(\vartheta)\,|0\rangle + \sin(\vartheta)e^{i\varphi}\,|1\rangle\,. \tag{1.2}$$

One can describe the state $|\psi\rangle$ as a vector

$$\begin{aligned}\vec{s} &= \langle\psi|\vec{\sigma}|\psi\rangle \\ &= \sum_j \langle\psi|\hat{\sigma}_j|\psi\rangle\, \hat{e}_j \\ &= \begin{pmatrix} \sin(2\vartheta)\cos(\varphi) \\ \sin(2\vartheta)\sin(\varphi) \\ \cos(2\vartheta) \end{pmatrix}\end{aligned} \tag{1.3}$$

in terms of the expectation value of the Pauli vector $\vec{\sigma} = \sum_j \sigma_j \hat{e}_j$. The components of the vector $\vec{s}$ are spherical coordinates on a sphere with radius 1, hence the projection of the state of a qubit can be visualized on a unit sphere [Lev08, p.237], called *Bloch sphere* (see Fig. 1.1).

One can express a quantum state $|\psi\rangle$ also as a *density matrix*

$$\rho = |\psi\rangle\langle\psi| \,. \tag{1.4}$$

The trace of a density matrix is $\mathrm{Tr}\{\rho\} = 1$. A quantum state that can be represented in the form Eq. (1.4) is called *pure state*, but the state of a system can also be the sum over an ensemble,

$$\rho = \sum_n p_n \, |\psi_n\rangle\langle\psi_n| \,, \tag{1.5}$$

where p_n is the probability of the system to be in state ψ_n. In such a *mixed state*, the state of the system cannot be represented as a vector $|\psi\rangle$ anymore. Examples for mixed states are thermal states, where the probability $p_n = \frac{\bar{n}^n}{(\bar{n}+1)^{n+1}}$ depends on the average phonon number $\bar{n}$. Density matrices for two-level systems can be visualized on a Bloch sphere as well.

1.1.2. Entanglement

Consider a state describing a system consisting of two initially independent subsystems A and B. This state can be written as outer product of the states describing the subsystems

$$|\psi\rangle = |\psi_\mathrm{A}\rangle \otimes |\psi_\mathrm{B}\rangle \,. \tag{1.6}$$

If the state of two coupled systems can be written as Eq. (1.6), the system is called *separable*. Rewriting the substates in a joint basis yields

$$|\psi\rangle = \sum_{jk} \underbrace{a_j b_k}_{c_{jk}} \left(|j\rangle \otimes |k\rangle\right). \tag{1.7}$$

If the amplitude of a state $|\psi\rangle = \sum_{jk} c_{jk} \left(|j\rangle \otimes |k\rangle\right)$ cannot be factored with respect to the two subsystems as in Eq. (1.6), in other words, if there exist no a_j, b_k such that $c_{jk} = a_j b_k \, \forall j, k$, then the state is called *entangled*.

There exist several measures for the amount of entanglement, of which one is the concurrence [Hor+09]. For pure two-qubit states, the concurrence can be written as

$$C = 2\sqrt{2\left(1 - \mathrm{Tr}\{\rho_A^2\}\right)}, \tag{1.8}$$

where $\rho_A = \mathrm{Tr}_B |\psi\rangle\langle\psi|$ is the reduced density matrix of the state $|\psi\rangle$ with respect to system A. A state for which $C = 1$ is maximally entangled, while a state with $C = 0$ is separable. For a state of the form

$$|\psi\rangle = \cos(\vartheta)\,|00\rangle + e^{i\varphi}\sin(\vartheta)\,|11\rangle \tag{1.9}$$

the concurrence becomes $C = \sin(2\vartheta)$, thus all states with $\vartheta = \frac{\pi}{2}$ are maximally entangled, regardless of the phase φ. Furthermore, as can be seen from Eq. (1.8), the entanglement of a state does not change under local unitary operations [PV06].

Bell states are maximally entangled states which span a basis in the Hilbert space of two qubits. The canonical Bell state, which is often presented as an example for a maximally entangled state, is

$$|\psi\rangle = \frac{1}{\sqrt{2}}\left(|00\rangle + |11\rangle\right). \tag{1.10}$$

When this state is measured separately in system A and system B (in the z-basis), the measurement outcome will always be the same for both systems, although the probability for each outcome (both 0 or both 1) is 50 %.

Any entangled state can be created from Bell states using local operations and

classical communication (LOCC), but not vice versa, because LOCC cannot increase entanglement [PV06]. This makes entanglement a resource under LOCC. It plays a crucial role in some quantum cryptography protocols [Eke91; BBM92], quantum teleportation [Ben+93], and superdense coding [BW92].

However, the extent to which entanglement contributes to quantum advantage remains topic of debate [Hor+09]. Ekert [EJM98] argues that while superposition could still be mimicked classically using waves, it is entanglement which makes the difference between a classical and quantum computer. Nonetheless, in quantum computing there exist protocols, for which entanglement is not needed [Bih+04] and in measurement-based quantum computing [RB01] entanglement can even reduce the speedup [GFE09]. However, although not being sufficient, entanglement is probably necessary for exponential speedup in most gate-based quantum computing protocols [JL03; LP01].

1.1.3. Universal gate set

A gate set is called *universal* if any unitary and consequently reversible operation can be approximated efficiently to an arbitrary degree of accuracy by a circuit that is composed solely of gates of the set [NC10]. A universal gate set consists, for example, of single qubit gates and one non-classical multi-qubit gate [DBE97].

Note that not all multi-qubit gates provide universality, but most do. Specifically, entangling gates always provide universality [Dod+02]. Moreover, the universality of entangling gates implies that any multi-qubit entangling gate can be replaced by a set of single-qubit operations and two-qubit entangling operations. For physical qubits, a typical choice for a gate set consists of single qubit rotations and a perfect entangler, while for logical qubits one often relies on the minimal set of Clifford gates complemented by a T gate [CTV17].

1.1.4. Propagation/evolution

The dynamics of a closed system, which is described by the Hamiltonian $\hat{H}$, is governed by the Schrödinger equation

$$i\hbar\partial_t \left|\psi(t)\right\rangle = \hat{H} \left|\psi(t)\right\rangle . \tag{1.11}$$

The solution for the state vector at any given time can be expressed as

$$|\psi(t)\rangle = \hat{U}(t, t_0)\,|\psi(t_0)\rangle\,, \tag{1.12}$$

where the unitary operator $\hat{U}$ is called *time development operator*. The general expression for the time development operator $\hat{U}(t, t_0)$ is given by

$$\hat{U}(t, t_0) = \mathcal{T}\exp\left\{-\frac{i}{\hbar}\int_{t_0}^{t}\hat{H}(\tau)\mathrm{d}\tau\right\}, \tag{1.13}$$

where $\mathcal{T}$ represents the time-ordering operator. In cases where the Hamiltonian $\hat{H}(t) = \hat{H}_0$ is time-independent, the time development operator simplifies to

$$\hat{U}(t, t_0) = \exp\left\{-\frac{i}{\hbar}\hat{H}_0(t - t_0)\right\}. \tag{1.14}$$

Nonetheless, for systems with time-dependent Hamiltonian, the expression for the time development operator depends on the particular structure of the Hamiltonian.

1.1.5. Platforms

Platforms for quantum computing compromise for example superconducting qubits, trapped ions or atoms, NV-centers, and photons. Recently, breakthroughs in error correction were demonstrated for superconducting qubits [Goo+25] and also for trapped-ion qubits [Pae+24]. These platforms meet the five criteria, proposed by DiVincenzo [DiV00], which describe conditions on a system that are needed for building a gate-based quantum computer [BCD02]. These criteria are:

a) Scalable qubits
The system must incorporate two-level subsystems that are capable of functioning as qubits. Furthermore, it should be feasible to scale up the number of qubits and establish efficient coupling between them. The challenge of scalability represents a significant obstacle in the development of quantum computing technology, due to the increasing complexity and difficulty of managing and controlling a growing number of qubits and their inter-

actions. In general, the number of controls increases with the number of qubits and introduces noise into the system, so manipulation of qubits while maintaining the quantum information becomes more challenging with escalating qubit number.

b) Qubit preparation

The accuracy of the outcome of a quantum protocol anticipates the existence of an initial qubit state which can be reliably prepared. This is because the initial state serves as the foundation for all subsequent quantum operations and any errors or inconsistencies in the initial state can propagate and accumulate throughout the computation, ultimately leading to significant reductions in the overall fidelity. Moreover, the initial state preparation must be fast to develop the full potential of quantum computing.

c) Readout

A quantum platform needs the capability to read out the state of specific qubits with minimal introduction of noise into the system. Due to the non-unitary nature of measurements, as opposed to unitary gate operations, they are always a potential source of noise, making effective readout protocols essential.

d) Universal gates

The quantum computing system must possess the ability to facilitate interactions between qubits in such a manner that the implementation of a universal gate set is possible. This is important, as a universal gate set provides the fundamental building blocks for performing arbitrary quantum operations on a set of qubits. The fidelity of the gates should be below the error correction threshold.

e) Long decoherence

The lifetime of the qubits must be long enough to allow for the completion of a quantum computation before decoherence and other sources of noise introduce errors and reduce the fidelity of the computation. Furthermore, it must be possible to improve the results by application of error correction and fault-tolerant quantum computation.

1.2. Trapped-ion platform

Trapped ions serve as a relevant platform for quantum computing. They allow for a large number of qubits [Mos+23] with long coherence times of about 1 s [Har+16; Hei+19]. Two-qubit gate durations are in the microsecond range.

The two most prevalent types of ion traps are Paul traps and Penning traps. Penning traps, proposed by Dehmelt in 1956 [Deh56], operate using static electrical and magnetic fields. In contrast, Paul developed in 1953 a mass spectrometer based on static and dynamic electrical fields [PS53]. This device could function as a mass filter as well as an ion trap, depending on the trap geometry and applied voltages. Initially, trapped ions were used primarily for quantum metrology such as atomic clocks [AV76]. The development of laser cooling [WI79] and of the Cirac-Zoller two-qubit gate [CZ95] paved the way towards quantum computing with trapped ions.

1.2.1. Linear Paul trap

In a Paul trap, ions are confined in a ultra high vacuum (UHV) environment using an oscillating radio frequency (RF)-field in conjunction with a static potential.

In a linear Paul trap, the confinement in x- and y-direction is usually created using four rod-shaped electrodes. In z-direction, the confinement is created by electrodes at the ends of the trap. Because the distance between center of the trap and the endcap electrodes is large compared to the distance between the rods, the potential in z-direction can be modeled approximately as the potential created by two point charges, each with charge q_z, separated by a distance $2z_0$. Expanding the potential around the origin $z = 0$ yields

$$\begin{aligned}\Phi_z &= \frac{1}{4\pi\varepsilon_0}\left(\frac{q_z}{z_0 - z} + \frac{q_z}{z_0 + z}\right) \\ &= \frac{q_z}{4\pi\varepsilon_0}\left(\frac{2}{z_0} + \frac{2}{z_0^3}z^2\right) + \mathcal{O}(z^4) \\ &= U_z\left(1 + \frac{z^2}{z_0^2}\right) + \mathcal{O}(z^4),\end{aligned} \tag{1.15}$$

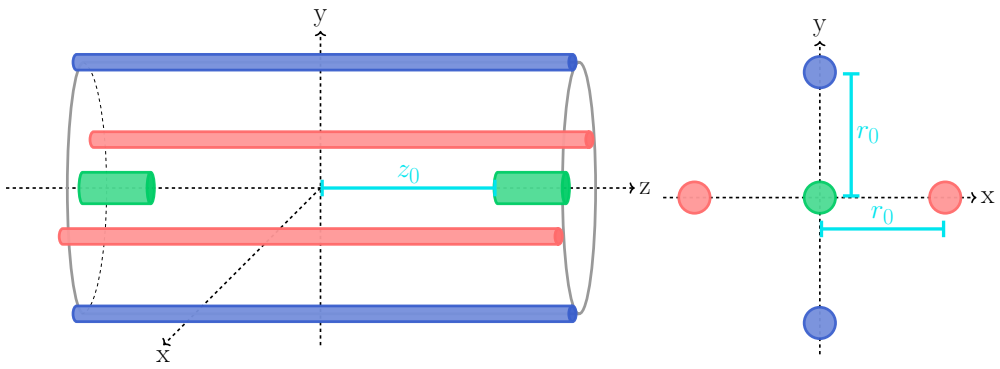

Figure 1.2.: Sketch of a linear Paul trap. (a) Side-view. An oscillating voltage is applied to the four rod-shaped electrodes surrounding the z-axis, with a phase difference of π between the voltages applied to the electrodes on the x-axis (orange) and those on the y-axis (blue). The static potential in the z-direction is created with the endcap electrodes on the z-axis (green). (b) Top-view of the Paul trap. The blue electrodes are on the y-axis and the orange electrodes on the x-axis.

with $U_z := \Phi_z(0)$. The constant part of the potential can be disregarded, resulting in a harmonic potential

$$\Phi_z = \frac{M}{2}\nu_z^2 z^2, \tag{1.16}$$

with M being the mass of the trapped particle and with the frequency of the motional mode

$$\nu_z = \sqrt{\frac{2U_z}{Mz_0^2}}. \tag{1.17}$$

The potential in the xy-plane can be seen as a quadrupole. Expanding this potential around $x, y = 0$ yields

$$\begin{aligned}\Phi_{xy} = \frac{1}{4\pi\varepsilon_0}\Bigg(&\frac{q_x}{\sqrt{y^2+(a_x+x)^2}} + \frac{q_x}{\sqrt{y^2+(a_x-x)^2}} \\ &+ \frac{q_y}{\sqrt{x^2+(a_y+y)^2}} + \frac{q_y}{\sqrt{x^2+(a_y-y)^2}}\Bigg) \\ = U_x + U_y &+ \frac{x^2}{r_0^2}\left(U_x - \frac{1}{2}U_y\right) + \frac{y^2}{r_0^2}\left(U_y - \frac{1}{2}U_x\right) + \mathcal{O}(x^4, y^4, x^2y^2).\end{aligned} \tag{1.18}$$

Again omitting constant terms, the total potential in the center of the trap can be described as

$$\Phi = \frac{x^2}{r_0^2}\left(U_x - \frac{1}{2}U_y\right) + \frac{y^2}{r_0^2}\left(U_y - \frac{1}{2}U_x\right) + \frac{z^2}{z_0^2}U_z =: \sum_j \frac{\alpha_j}{2}x_j^2, \tag{1.19}$$

with $\alpha_z = \frac{U_z}{z_0^2}$, $\alpha_x = \frac{2U_x - U_y}{2r_0^2}$, $\alpha_y = \frac{2U_y - U_x}{2r_0^2}$.

Considering an ion of mass M and atomic number Z in the trap, the Lagrangian is given by

$$\mathcal{L} = \sum_j \left(\frac{M}{2}\dot{x}_j^2 - \frac{Ze}{2}\alpha_j x_j^2\right), \tag{1.20}$$

and the resulting equations of motion are

$$\ddot{x}_j + \frac{Ze}{M}\alpha_j x_j = 0. \tag{1.21}$$

Assuming only static potentials, a solution for Eq. (1.21) would be of the form

$$x_j(t) = Ae^{i\omega_j t} + Be^{-i\omega_j t} \tag{1.22}$$

with $\omega_j^2 = \frac{Ze}{M}\alpha_j$. This yields a harmonic motion only if $\alpha_j > 0$ (in the case of a positively charged ion), otherwise x_j diverges. However, close to the trap center there are no charge sources, and thus $\vec{\nabla} \cdot \vec{E} = 0$, yielding the Laplace equation $\Delta\Phi = \sum_{j=x,y,z} \alpha_j = 0$. Fulfilling this condition is only possible if at least one $\alpha_j < 0$, which contradicts the condition $\alpha_j > 0$ in the case of a static field, as stated above. In view of this, *Earnshaw's theorem* states that it is not possible to confine charged particles in a purely static electric potential [Foo+05]. Thus, for confinement of charged particles with electromagnetic fields, time-dependent electric potentials (Paul trap) or magnetic fields (Penning trap) are required.

To investigate the motion of particles in a Paul trap we replace $U_j = U_j^{\mathrm{DC}} + U_j^{RF}\cos(\Omega_{\mathrm{RF}}t)$. The equations of motion Eq. (1.21) become

$$\ddot{x}_j + \left(\frac{Ze}{M}\alpha_j^{\mathrm{DC}} + \frac{Ze}{M}\alpha_j^{\mathrm{RF}}\cos(\Omega_{\mathrm{RF}}t)\right)x_j = 0. \tag{1.23}$$

For a static potential this results in the same equations of motion as Eq. (1.21),

but for non-static potentials, this equation has the form of a Mathieu equation [Sin14]. The solutions of this type of equations can be stable or unstable, depending on the values of the parameters [AS72].

A simple approximate solution can be derived if the frequency of the RF-field is large compared to the frequency of the unperturbed system: $\Omega_{\mathrm{RF}}^2 \gg \frac{Ze}{M}\alpha_j^{\mathrm{DC,\,RF}}$ [RGF03]. We assume that we can split the coordinate $x(t)$ into a slowly oscillating part $X(t)$ and a perturbation $\xi(t)$ oscillating at frequency Ω_{RF} (and omitting the index j).

Inserting $x(t) = X(t) + \xi(t)$ into Eq. (1.23) and sorting by oscillation frequency and amplitude yields

$$\underbrace{\ddot{X} + \frac{Ze}{M}\alpha_{\mathrm{DC}}X}_{\text{slowly oscillating}} + \underbrace{\frac{Ze}{M}\alpha_{\mathrm{RF}}\cos(\Omega_{\mathrm{RF}}t)X + \ddot{\xi}}_{\text{fast oscillation and large amplitude}} + \underbrace{\frac{Ze}{M}\alpha_{\mathrm{DC}}\xi + \frac{Ze}{M}\alpha_{\mathrm{RF}}\cos(\Omega_{\mathrm{RF}}t)\xi}_{\text{fast oscillation and small amplitude}\mathcal{O}(\xi)} = 0. \tag{1.24}$$

We assume that we can treat the parts of the equation separately. First, look at the large fast oscillating part

$$\ddot{\xi} = -\frac{Ze}{M}\alpha_{\mathrm{RF}}X\cos(\Omega_{\mathrm{RF}}t). \tag{1.25}$$

Since the coordinate X is changing on a significantly slower timescale that ξ, we can assume it to be constant for the integration. In this case, the solution for Eq. (1.25) is

$$\xi(t) = \frac{Ze}{M\Omega_{\mathrm{RF}}^2}\alpha_{\mathrm{RF}}X\cos(\Omega_{\mathrm{RF}}t). \tag{1.26}$$

As demanded by the above conditions, ξ oscillates with frequency Ω_{RF} compared to X, and it is smaller than X by a factor $\Omega_{\mathrm{RF}}^2\frac{M}{Ze}\alpha_{\mathrm{RF}} \gg 1$. We see that the total motion is described by

$$x(t) = X(t)\left(1 + \frac{Ze}{M\Omega_{\mathrm{RF}}^2}\alpha_{\mathrm{RF}}\cos(\Omega_{\mathrm{RF}}t)\right), \tag{1.27}$$

where the slow part $X(t)$ is called *secular motion* and the oscillatory part *micromotion*.

To find an expression for the secular motion $X(t)$, we insert Eq. (1.26) back into Eq. (1.24) and average out all quickly oscillating functions, that is, we replace $\sin(\Omega_{\mathrm{RF}}t)$ and $\cos(\Omega_{\mathrm{RF}})$ by their average 0, and, analogously, $\cos^2(\Omega_{\mathrm{RF}}t)$ by $\frac{1}{2}$. This yields the equation of motion

$$\ddot{X} + \frac{Ze}{M}\underbrace{\left(\alpha_{\mathrm{DC}} + \frac{Ze\alpha_{\mathrm{RF}}^2}{M^2\Omega_{\mathrm{RF}}^2}\right)}_{\alpha_{\mathrm{eff}}} X = 0. \tag{1.28}$$

Hence, the ion moves as if it was subject to an effective potential [MD68]

$$\Phi_{\mathrm{eff}} = \frac{1}{2}\alpha_{\mathrm{eff}}x^2 = \Phi_{\mathrm{DC}} + \frac{Ze}{M\Omega_{\mathrm{RF}}^2}\Phi_{\mathrm{RF}}^2. \tag{1.29}$$

The effective potential can be harmonic, with $\alpha_{\mathrm{eff}} > 0$, while at the same time the Laplace equation for the system

$$\Delta\Phi = \sum_{j=x,y,z} \alpha_j^{\mathrm{DC}} + \cos(\Omega t) \sum_{j=x,y,z} \alpha_j^{RF} = 0 \tag{1.30}$$

is fulfilled. In a linear Paul trap, one can choose, as an example, $\alpha_x^{\mathrm{RF}} = -\alpha_y^{\mathrm{RF}}$, corresponding to a phase shift of π between the voltages of the rods in x- and y-direction [SQ17]. The static potential fulfills the Laplace equation when $\alpha_x^{\mathrm{DC}} + \alpha_y^{\mathrm{DC}} = -\alpha_z^{\mathrm{DC}}$, for instance [RGF03].

The linear Paul trap is not the only design of a Paul trap. There are many more setups, including hyperbolic Paul traps, which use hyperbolic rings, and surface traps, where the electrodes are printed on a circuit chip [PKL22]. Also, instead of using oscillating UHV-fields, one can apply strong magnetic fields, as is done in a Penning trap [Jai+24].

Generalizing from the type of the trap, we consider now a chain of ions trapped in an (approximately) harmonic potential, since the results of this work can be applied to any trap that creates confinement in a harmonic potential in z-direction, as long as the motion in the other directions can be neglected.

1.2.2. Qubits

In a trapped-ion trap quantum computer architecture, the qubits consist of two specific levels in the atomic structure of the ion. Examples of ions that are used in quantum computing experiments include $^{43}Ca^{+}$[Ben+08a; Mye+08; Sch+18], $^{40}Ca^{+}$ [Cla+21; Meh+19; Mye+08], $^{9}Be^{+}$ [Gae+16; Zar+19], $^{171}Yb^{+}$ [Olm+07], $^{111}Cd^{+}$ [Sti+06], and $^{25}Md^{+}$ [Osp+11].

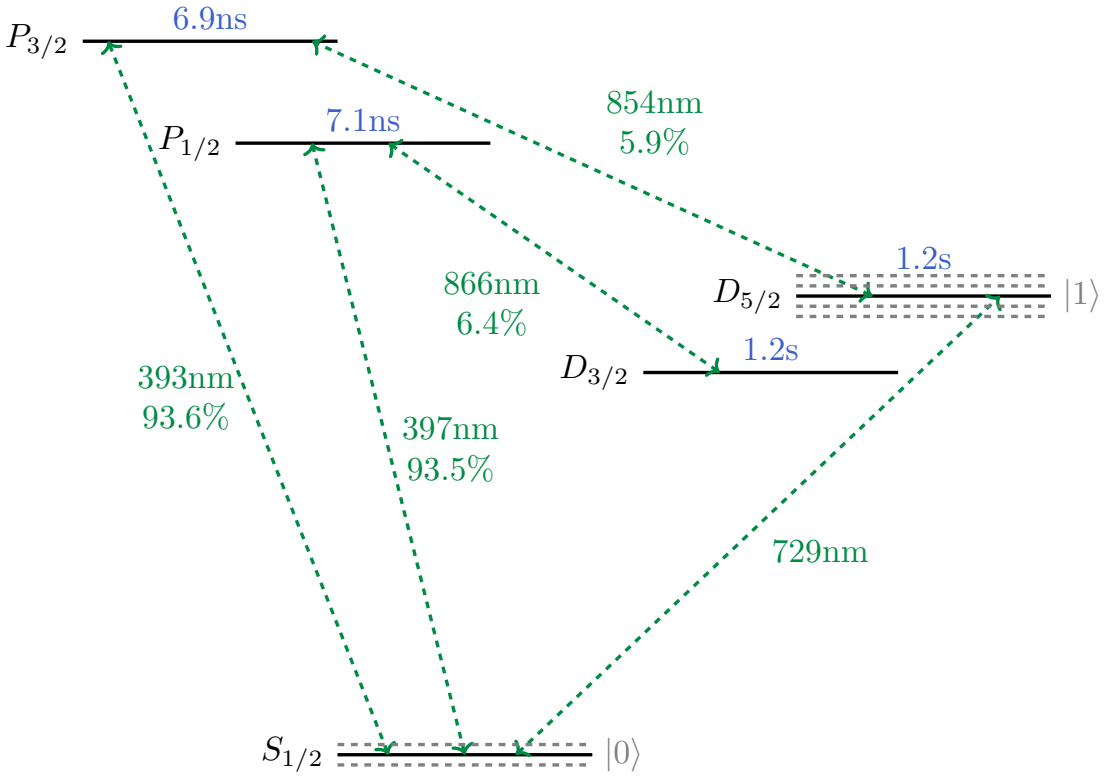

Figure 1.3.: Level scheme of $^{40}Ca^{+}$ (reproduced from [Hei+19]). The optical qubit is encoded in the fine structure levels $S_{1/2}$ and $D_{5/2}$. The transition $S_{1/2}$–$P_{1/2}$ can be used for cooling. For initialization, the excited state $D_{5/2}$ is pumped to $P_{3/2}$, which then decays with high probability to the ground state. As the P-levels decay also into $D_{3/2}$, the transition between this level and $P_{3/2}$ needs to be pumped as well for initialization to avoid population loss. For readout, one can pump the transition $S_{1/2}$–$P_{1/2}$ and observe the subsequent fluorescence.

As an example, the level scheme of $^{40}Ca^{+}$ is shown in Fig. 1.3. Here, the qubit is stored in the $S_{1/2}$ and $D_{5/2}$ level [Mye+08]. The $D_{5/2}$-level is chosen, because it has a lifetime of the order of 1 s [Kre+05].

$^{40}Ca^+$ is an example for an ion species used for *optical qubits*, where the qubit is encoded in the fine structure levels of the ions (as an example, take $S_{1/2}$ as ground state and the meta-stable state $D_{5/2}$ as excited state). Their transition wavelength lies in the optical range (for the given example $^{40}Ca^+$ it is 729 nm). It is also possible to encode qubits in the hyperfine levels, this other type of qubits is hence called *hyperfine qubit*. The typical wavelength for hyperfine qubits lies in the microwave range. As an example, the qubit wavelength for $^{43}Ca^+$ is 9.4 cm [Bal+16].

Cooling

To prevent undesirable excitations in the motional mode, to assure that the ions remain at the center of the trap, and to ensure the validity of the approximations made in Section 1.2.1, it is essential to cool the ions to a low-energy motional state. This also facilitates control and observation of the ions.

Laser cooling [Ita+91] involves driving the ions with laser beams, in such a way that on average the number of phonons in the motional mode is reduced. The methods depend on the available level spacing and thus on the specific ion species.

If the linewidth Γ of the electronic transition that is used for cooling is large compared to the frequency of the motional modes, *Doppler cooling* can be used [Esc+03]. This technique involves a laser that is detuned slightly below a transition frequency of the ion. As the ions move, they experience a frequency shift due to the Doppler effect. An ion that moves towards the laser beam such that the Doppler-shifted laser frequency matches exactly the transition frequency may absorb a photon which is then re-emitted in a random direction. Consequently, the average velocity of the ions decreases, resulting in a cooling effect. Nevertheless, Doppler cooling is limited by the linewidth Γ of the transition. The Doppler temperature, which is a measure for the minimal achievable temperature using Doppler cooling, is $T_D = \hbar\frac{\Gamma}{2k_B}$, where k_B is the Boltzmann constant.

To surpass this limitation, the use of additional cooling strategies is needed. The electronic transition can also be chosen in such a way that $\Gamma \ll \nu$. In this regime, the energy levels of the motional mode are resolved, which enables *sideband cool-*

ing [Neu+78]. Here, the laser is detuned to the red sideband frequency (see Section 1.2.3), which is a transition that excites the electronic mode of the ion while simultaneously decreasing its vibrational mode number. Since the decay rate Γ of the electronic mode is larger than the decay rate of the motional mode, the electronic mode decays spontaneously, while the phonon number of the vibrational mode either is increased or decreased by one or remains unaltered. Consequently, the average vibrational number is reduced, leading to a decrease in the vibrational energy. Theoretically, this and other cooling methods allow cooling to the vibrational ground state of the ion [Win+98].

Optical pumping

Optical pumping [Kas50] is used for initialization as well as for excitation of the qubits. During the initialization phase, the qubits are prepared in their ground state by coupling the excited state to an auxiliary shelf state, which subsequently decays rapidly to the ground state. For example, in $^{40}Ca^{+}$ ions (see Fig. 1.3), the lifetime of the shelf state ($P_{3/2}$) is $\approx 7\,\mathrm{ns}$, compared to a lifetime of $\approx 1.2\,\mathrm{s}$ of the excited state ($D_{5/2}$), enabling fast initialization.

Readout

The readout process is carried out with *electron shelving* [NSD86], where a strong laser stimulates the transition between one of the qubit states and a designated shelf state. For fast readout (as for fast initialization), a short lifetime of the shelf state is required. If the shelf state decays not exclusively to the qubit state, but also significantly to another state, this other transition is driven as well, repumping the population to the shelf state. As the shelf state decays back to the qubit state, observation of fluorescence can indicate population of the specific qubit state. If the transition between qubit state and shelf state is not near to a resonance of the other qubit state, fluorescence is only observed for one of the states, which is therefore called *bright state*. In contrast, the other qubit state is called *dark state*. Specifically, for the case of $^{40}Ca^{+}$, the bright state is the ground state of the qubit and can be detected by driving the $S_{1/2} - P_{1/2}$ and $D_{3/2} - P_{1/2}$ transitions (see Fig. 1.3).

1.2.3. Single-qubit gates

Control and manipulation of quantum states in trapped-ion quantum computers are typically performed using laser beams [Win+98]. The interaction between a monochrome driving field and a two-level system, with Pauli X operator $\hat{\sigma}_x$ and position operator $\hat{q}$, can be described with the general Hamiltonian for a dipole interacting with a radiation field [CDG98; Win+98]

$$\hat{H}_{\text{int}} = \vec{d} \cdot \vec{E} = 2\hbar\Omega\hat{\sigma}_x \cos(k\hat{q}\cos(\vartheta) - \omega_L t + \varphi), \tag{1.31}$$

where k is the wave number, ϑ the angle of the wave vector, ω_L the frequency, and φ the phase of the drive.

We assume that the drive field and the dipole are aligned in the same direction ($\vartheta = 0$).

As described in Section 1.2.1, the movement of a trapped ion can be described approximately as movement of a particle in an effective harmonic potential. This potential, which we derived classically, can be treated quantum mechanically as well, with the corresponding Hamiltonian

$$\hat{H}_{\text{motion}} = \frac{1}{2M}\hat{p}^2 + \frac{M}{2}\nu^2\hat{q}^2, \tag{1.32}$$

where ν denotes the frequency of the corresponding motional mode. Introducing the creation and annihilation operators $\hat{a}^\dagger$ and $\hat{a}$, we can express the position operator as

$$\hat{q} = \sqrt{\frac{\hbar}{2M\nu}}\left(\hat{a} + \hat{a}^\dagger\right). \tag{1.33}$$

For multiple ions in a trap, the motion of the ions can be described in terms of motional modes, each with frequency ν_p and associated annihilation and creation operators $\hat{a}_p$, $\hat{a}_p^\dagger$ [Jam98]. For a chain with only two ions, there are only two motional modes, the motion of the center of mass (COM), and the relative motion, the breathing mode (BM). The frequencies of these motional modes are related by

$$\nu_{\text{BM}} = \sqrt{3}\nu_{\text{COM}}. \tag{1.34}$$

In the following calculations, we consider only one of the motional modes for the sake of simplicity, without loss of generality.

Inserting the expression for the position operator in Eq. (1.33) into the Hamiltonian in Eq. (1.31) and moving into an interaction picture with respect to the qubit and the motional mode, the interaction Hamiltonian becomes

$$\hat{H} = \frac{\hbar}{2}\Omega\left(\hat{\sigma}_+ e^{i\omega_q t} + \hat{\sigma}_- e^{-i\omega_q t}\right)\left(e^{i\left(\eta\left(\hat{a}^\dagger e^{i\nu t} + \hat{a}e^{-i\nu t}\right) - \omega_L t + \varphi\right)} + e^{-i\left(\eta\left(\hat{a}^\dagger e^{i\nu t} + \hat{a}e^{-i\nu t}\right) - \omega_L t + \varphi\right)}\right), \tag{1.35}$$

where we used the Lamb-Dicke factor, defined as

$$\eta = k\sqrt{\frac{\hbar}{2M\nu}}, \tag{1.36}$$

and the Pauli ladder operators $\hat{\sigma}_\pm = \hat{\sigma}_x \pm i\hat{\sigma}_y$.

If the detuning $\delta = \omega_q - \omega_L$ of the drive is small relative to the qubit frequency $\delta \ll \omega_q$, the Hamiltonian can be approximated in a rotating-wave approximation (RWA) as

$$\hat{H} = \frac{\hbar}{2}\Omega\left(\hat{\sigma}_+ e^{i\left(\eta\left(\hat{a}^\dagger e^{i\nu t} + \hat{a}e^{-i\nu t}\right) - \delta t + \varphi\right)} + \hat{\sigma}_- e^{-i\left(\eta\left(\hat{a}^\dagger e^{i\nu t} + \hat{a}e^{-i\nu t}\right) - \delta t + \varphi\right)}\right). \tag{1.37}$$

When the Lamb-Dicke factor is small, indicating weak coupling between electronic and motional modes, the Hamiltonian Eq. (1.31) can be approximated by [Lei+03]

$$\hat{H} = \frac{\hbar}{2}\Omega\left(\hat{\sigma}_+ e^{-i\delta t + i\varphi} + \hat{\sigma}_- e^{i\delta t - i\varphi}\right) + i\frac{\hbar}{2}\Omega\eta\left(\hat{a}^\dagger e^{i\nu t} + \hat{a}e^{-i\nu t}\right)\left(\hat{\sigma}_+ e^{-i\delta t + i\varphi} - \hat{\sigma}_- e^{i\delta t - i\varphi}\right). \tag{1.38}$$

Driving at resonance with the qubit $\delta = 0$ is known as *carrier* drive, which has the Hamiltonian

$$H_{\text{carrier}} = \frac{\hbar}{2}\Omega\hat{\sigma}_x \cos\varphi, \tag{1.39}$$

where we have neglected oscillating terms. From Eq. (1.39), we see that the carrier drive yields a single qubit gate without affecting the motional mode.

When the laser is detuned from the qubit by the motional mode frequency $\delta = \nu$,

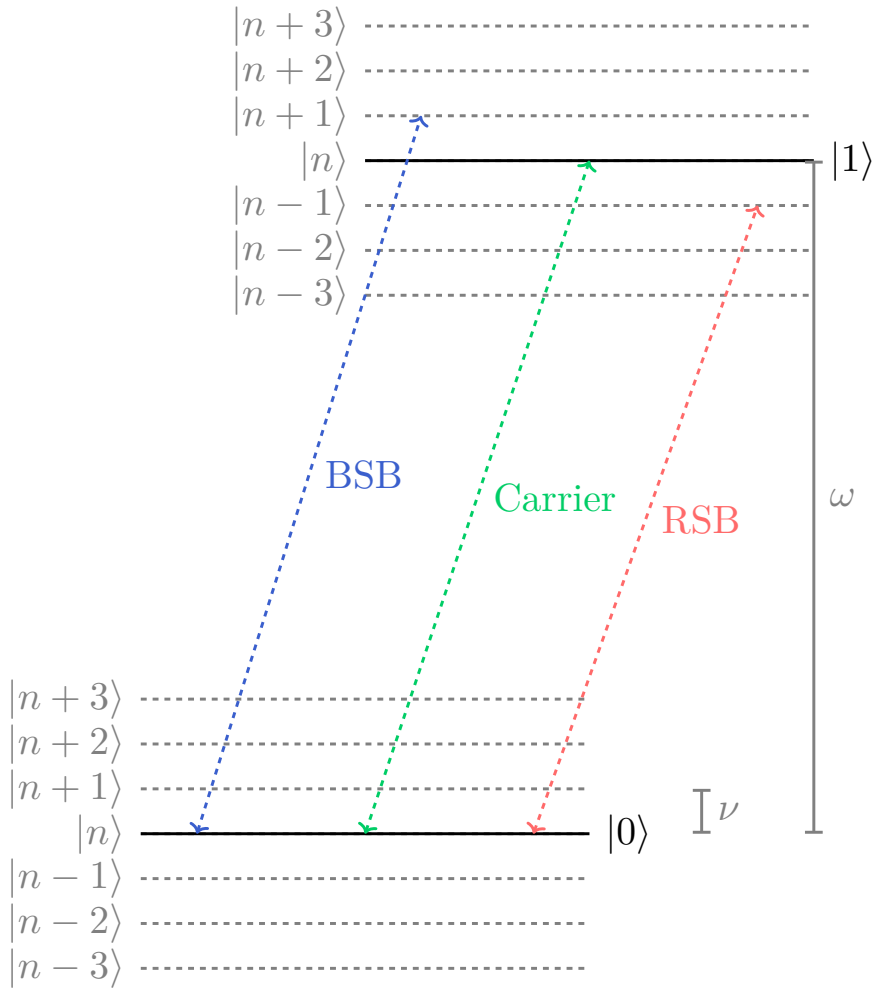

Figure 1.4.: Carrier and sideband drives. The carrier drive (green, in the middle) is a drive with frequency ω_q, hence, it drives the transition between the qubit levels without affecting the motional modes. The blue and red sideband (blue line on the left and red line on the right, respectively) is a drive detuned from the qubit frequency by $\delta = +\nu$ and $\delta = -\nu$ respectively, which drives a qubit transition while changing the phonon number of the motional mode by ± 1.

the Hamiltonian approximates (again omitting oscillating terms) to

$$\hat{H}_{\mathrm{BSB}} = \frac{\hbar}{2}\Omega\eta i\left(\hat{\sigma}_+\hat{a}^\dagger e^{i\varphi} - \hat{\sigma}_-\hat{a}e^{-i\varphi}\right). \tag{1.40}$$

Driving the *blue sideband (BSB)* thus yields an excitation of the qubit and the motional mode at the same time. Analogously, driving at $\delta = -\nu$ yields an approx-

imate Hamiltonian

$$\hat{H}_{\mathrm{RSB}} = \frac{\hbar}{2}\Omega\eta\left(\hat{\sigma}_{+}\hat{a}e^{i\varphi} + \hat{\sigma}_{-}\hat{a}^{\dagger}e^{-i\varphi}\right), \tag{1.41}$$

which means that the *red sideband (RSB)* yields an excitation of the qubit while decreasing the phonon number in the motional mode by one. The carrier and sideband drive transitions are illustrated in the energy diagram of Fig. 1.4.

1.2.4. Two-qubit gates

The first entangling gate that was invented for trapped-ion qubits, is the Cirac-Zoller gate[CZ95]. It uses the RSB-transition and an auxiliary state.

Applying a pulse of length $T = \frac{k\pi}{\eta\Omega}$ on a qubit in a state $|e\rangle$ or $|g\rangle$ and with motional mode in state $|0\rangle$ or $|1\rangle$, results in the transitions

$$\begin{aligned} |0,e\rangle &\rightarrow \cos\left(\frac{k\pi}{2}\right)|0,e\rangle - e^{-i\varphi}\sin\left(\frac{k\pi}{2}\right)|1,g\rangle \\ |1,g\rangle &\rightarrow \cos\left(\frac{k\pi}{2}\right)|1,g\rangle + e^{i\varphi}\sin\left(\frac{k\pi}{2}\right)|0,e\rangle\,. \end{aligned} \tag{1.42}$$

The procedure for the Cirac-Zoller gate is the following. The system is cooled down to the ground state of the motional mode, then the following series of operations is applied [HRB08]:

1. A π-pulse on the RSB, with length $\frac{\pi}{\eta\Omega}$ ($k = 1$), is applied to the first qubit. If the motional mode is in the ground or first excited state, the pulse has no effect, unless the qubit electronic state is excited $|e\rangle$ and the motional mode in the ground state $|0\rangle$, or vice versa with the ion in the electronic ground state $|g\rangle$ and in the first excited state of the motional mode $|1\rangle$. In the first case, the electronic state flips to the ground state while exciting the trap, catching a phase a $-e^{-i\varphi}$, and in the second case the opposite occurs, with an additional phase $e^{i\varphi}$.

$$\begin{aligned} |0e_1\rangle &\rightarrow -e^{-i\varphi}|1g_1\rangle \\ |1g_1\rangle &\rightarrow \quad e^{i\varphi}|0e_1\rangle \end{aligned} \tag{1.43}$$

2. The ground state of the second qubit is coupled to an auxiliary state via a 2π-pulse on the RSB, with length $\frac{2\pi}{\eta\Omega}$ ($k = 2$). This operation flips the sign of the state $|1g_2\rangle$ for the second qubit.

$$|1g_2\rangle \rightarrow \quad -|1g_2\rangle \tag{1.44}$$

3. Same as step 1. A π-pulse, identical to the one in step 1, is applied to the first qubit.

By examining the possible states, we find that the Cirac-Zoller gate leaves all states that start in the ground state of the motional mode unchanged, except when both qubits are initially in the excited state, in which case a phase of -1 is added.

$$\begin{aligned}
|0gg\rangle &\rightarrow & |0gg\rangle &\rightarrow & |0gg\rangle &\rightarrow & |0gg\rangle \\
|0ge\rangle &\rightarrow & |0ge\rangle &\rightarrow & |0ge\rangle &\rightarrow & |0ge\rangle \\
|0eg\rangle &\rightarrow & e^{-i\varphi}|1gg\rangle &\rightarrow & -e^{-i\varphi}|1gg\rangle &\rightarrow & |0eg\rangle \\
|0ee\rangle &\rightarrow & e^{-i\varphi}|1ge\rangle &\rightarrow & e^{-i\varphi}|1ge\rangle &\rightarrow & -|0ee\rangle
\end{aligned} \tag{1.45}$$

Therefore, the Cirac-Zoller gate implements a CZ-gate.

Despite being implemented experimentally [Sch+03a], the Cirac-Zoller gate has the disadvantage of relying on the motional mode to be cooled down to its ground state, which is challenging to reach in experiment.

An alternative two-qubit gate for trapped ions, which is inherently more robust with respect to heating of the motional modes, was proposed by Sørensen and Mølmer in 1999 [SM99] and further expanded in 2000 [SM00]. The Mølmer-Sørensen gate works by driving the RSB and the BSB on both ions at the same time, resulting in a two photon transition exciting both ions without significantly affecting the motional modes. The Mølmer-Sørensen gate will be explained and discussed in the second part of this thesis.

Chapter 2.

Correction formulas for the Mølmer-Sørensen gate

A ubiquitous aspect of quantum processor design is the need to provide a strong contrast, or on-off ratio, between entanglement coupling versus idling and local single-qubit gates. To this effect, the standard approach is to introduce new coupling elements, whose auxiliary Hilbert space provides a means through which entanglement can temporarily be mediated, for example, via intermediate cavity bus [Pai+16; HK21; LCM24], nonlinear resonators [Bar+19; Rea+18; Neg+21], motional trapping modes [Sch+03b; Ben+08b; Sch+18; Meh+19; Cla+21; KCM22; Web+24], intermediary spins [Fei+12; CWP17], etc.

To fully leverage these coupling elements, and avoid the onset of decoherence, it is desirable to turn on the effective coupling between qubits as strongly as possible, for example through the use of strong driving fields. The prototypical example of this is the so-called Mølmer-Sørensen gate. This technique was first introduced in Ref. [SM99] to be resilient against trap heating within the Lamb-Dicke and weak driving perturbative approximations [LM20; Arr+18; Ber+12; Coh+15; Jia+23; Val+22; Kan+21]. And yet, it is important to recognize that wide adoption of the gate largely occurred after a further advancement, whereby strong driv-

This chapter was published in similar form as "Susanna Kirchhoff, Frank K. Wilhelm, and Felix Motzoi. 'Correction Formulas for the Mølmer-Sørensen Gate Under Strong Driving'. Version 2. In: *PRX Quantum* 6.1 (Feb. 12, 2025), p. 010328. DOI: 10.1103/PRXQuantum.6.010328" by the American Physical Society under the terms of the Creative Commons Attribution 4.0 International license. The majority of research was conducted and the majority of the text written by Susanna Kirchhoff.

ing could be reinstituted at the cost of the collective ion motion being temporarily activated before returning to its initial state [SM00].

In the wider context of trapped-ion quantum computing [Sch+13; HRB08; BKM16], the platform has blossomed to one of the leading candidates for housing quantum information, boasting long coherence times around 1 s to 50 s [Kau+17; Har+16], and infidelities for two-qubit gates on the order of 1×10^{-3} at a gate duration of 1.6 µs to 300 µs [Sch+18; Meh+19; Cla+21; Ben+08b].

Further advancements hinge on a proper theoretical understanding of the effect of strong driving on the operation with proper accounting of the excitation of the oscillator states, and potentially reduced gate duration. As with the oscillator-based couplings in other platforms, there are limited toolboxes available for tracking the dynamical effects of strong driving, the two most common being the Dyson and Magnus expansions. In the Mølmer-Sørensen gate, the standard argument, dating back 25 years to Ref. [SM00], argues that, within the Lamb-Dicke approximation, an effective Hamiltonian in the Magnus expansion leads to only a single order being nonzero and accounting for the entanglement. The gate itself is second order in the Lamb-Dicke parameter η, while the error is fourth order in η, appearing in the same Magnus order, and so dictates the ultimate error scaling of the gate.

In this chapter, we demonstrate that, in contrast to the standard argument, there are multiple nonzero $\mathcal{O}(\eta^2)$ terms in the effective Hamiltonian that can contribute even more significantly to the gate error than the $\mathcal{O}(\eta^4)$ error terms. These errors are higher order in the Rabi frequency, but since at strong driving this cannot be considered a small parameter (compared especially to the sideband detuning), these are fundamental to the functioning of the gate. We show that, in general, neglecting these terms leads to large detectable errors and deviations from experiment. These translate for typical parameters to circa 10 % Rabi frequency mismatch, and, without *in situ* recalibration, 10 to 100 times larger error than theoretically predicted.

We provide analytical expressions for the leading orders of those terms and give a correction term for the drive strength Ω which can partially compensate for the error caused by those terms. Our model results in a bound on the gate infidelity of about 10^{-3} for typical parameters, which matches well with experimental fi-

delity measurement results [Bal+16; Sch+18; Meh+19; Ger+22; Mos+23; San+23]. We also motivate analytically and show numerically, how it is—depending on the parameter regime—of advantage to use pulse shaping to improve the gate fidelity closer to 10^{-4}. This can help to approach fidelities needed for fault-tolerant quantum computing [Ber+17; Zar+19].

2.1. Model and methods

2.1.1. Time propagation

To begin with, we discuss the general methodology for obtaining the time propagation of our driven system. We want to first emphasize that for a system such as the Mølmer-Sørensen gate, the drive dependence cannot, in general, be described with perturbation theory, since it may be larger than other relevant energy scales. Therefore, where multiple small parameters may exist, these different contributions should be properly accounted to avoid early truncation.

To this end, we describe the three most common expansions to obtain the time evolution operator $\hat{U}(T)$ of a quantum system that gives the time evolution between time 0 and time T.

Trotter expansion

The Trotter expansion [Tro59] can be used especially for numerical purposes. For this, the evolution is sliced into small time steps during which one assumes the Hamiltonian to be approximately constant. To ensure this, it is recommendable to choose the time step Δt around an order of magnitude smaller than the inverse of the maximal frequency arising in the Hamiltonian $\Delta t \ll \frac{1}{f_{\max}}$. The time evolution operator $\hat{U}$ can then be decomposed into a product of time evolution operators from t to $t + \Delta t$

$$\begin{aligned}\hat{U}(t, t_0) &= \prod_{n=0}^{N_t} \hat{U}(t_0 + n\Delta t, t_0 + (n+1)\Delta t) \\ &= \prod_{n=0}^{N_t} \exp\left\{-\frac{i}{\hbar}\hat{H}(t_0 + n\Delta t)\Delta t\right\},\end{aligned} \tag{2.1}$$

where the product $\prod$ multiplies from right to left.

Dyson expansion

The Dyson expansion [ST94] expands the exponent in Eq. (1.13) and gives the time evolution operator as

$$\hat{U}(t,t_0) = \mathbb{1} + \sum_{k=1}^{\infty} \hat{P}_k(t,t_0), \tag{2.2}$$

where each term of the Dyson sum can be written as a time-ordered integral

$$\hat{P}_k(t,t_0) = \left(-\frac{i}{\hbar}\right)^k \int_{t_0}^{t} \mathrm{d}t_1 \int_{t_0}^{t_1} \mathrm{d}t_2 \cdots \int_{t_0}^{t_{k-1}} \mathrm{d}t_k \hat{H}(t_1)\hat{H}(t_2)\cdots\hat{H}(t_k). \tag{2.3}$$

The Dyson expansion works well for Hamiltonians that consist of a time-independent term and a perturbative time-dependent term: $\hat{H} = \hat{H}_0 + \Omega\hat{H}_1(t)$ with small Ω. In this case, the sum in Eq. (2.3) can be cut off, since higher-order terms can be neglected

$$\hat{U}(t,t_0) = \mathbb{1} - \frac{i}{\hbar}\Omega \int_{t_0}^{t} \mathrm{d}t_1 \hat{H}(t_1) + \frac{1}{2\hbar^2}\Omega^2 \int_{t_0}^{t} \mathrm{d}t_1 \int_{t_0}^{t_1} \mathrm{d}t_2 \hat{H}(t_1)\hat{H}(t_2) + \mathcal{O}(\Omega^3). \tag{2.4}$$

We want to emphasize that perturbation theory and the Dyson expansion are not generally suitable to describe the Mølmer-Sørensen gate appropriately, since the driving amplitude, which signifies the perturbation parameters here, is only small in the case of weak driving. In the strong driving limit, the Dyson expansion is thus not a reliable method to calculate the time evolution for this system.

Magnus expansion

An expansion with somewhat better convergence properties is the Magnus expansion [Mag54]. It is exact for example for the linearly driven oscillator and often converges quickly for fast oscillating systems, as it is the case here. Magnus expresses the time-evolution operator $\hat{U}(T)$ in terms of a time-independent

effective Hamiltonian

$$\hat{H}_{\text{eff}} = \sum_{k=1}^{\infty} \hat{Z}_k(T), \tag{2.5}$$

such that the time evolution operator [War84]

$$\hat{U}(T) = e^{-i\hat{H}_{\text{eff}}} \tag{2.6}$$

yields after time T the same dynamics as the time evolution operator of the original time-dependent Hamiltonian. The Magnus series expands the effective Hamiltonian into a sum, with the first three Magnus orders being

$$\begin{aligned}
\hat{Z}_1 &= \frac{1}{\hbar}\int_0^T dt \hat{H}(t) \\
\hat{Z}_2 &= \frac{i}{2\hbar^2}\int_0^T dt \int_0^t d\tau \left[\hat{H}(t), \hat{H}(\tau)\right] \\
\hat{Z}_3 &= -\frac{1}{6\hbar^3}\int_0^T dt \int_0^t d\tau \int_0^\tau d\tau' \left(\left[\left[\hat{H}(t), \hat{H}(\tau)\right], \hat{H}(\tau')\right]\right. \\
&\quad \left. + \left[\hat{H}(t), \left[\hat{H}(\tau), \hat{H}(\tau')\right]\right]\right).
\end{aligned} \tag{2.7}$$

There are also formulas for higher orders [Bla+09], which are omitted here due to their length. A recursive formula for all orders of the Magnus expansion is given in [Bla+09], and a general analytic expression for each order is given in [ACC18].

Salzmann [Sal85] suggests an alternative formula, which expresses the orders of the Magnus expansion in terms of different orders of the Dyson expansion. Using his result, one can easily show that the relations between the first three orders of Magnus and Dyson expansion are

$$\begin{aligned}
\hat{Z}_1 &= i\hat{P}_1 \\
\hat{Z}_2 &= i\hat{P}_2 - \frac{i}{2}P_1^2 \\
\hat{Z}_3 &= i\hat{P}_3 - \frac{i}{2}\left(P_1P_2 + P_2P_1\right) + \frac{i}{3}P_1^3.
\end{aligned} \tag{2.8}$$

If the first order of both Magnus and Dyson series are zero, $\hat{Z}_1 = i\hat{P}_1 = 0$, the

expressions simplify, with the first five orders of the Magnus expansion being

$$\begin{aligned}
\hat{Z}_2 &= i\hat{P}_2 \\
\hat{Z}_3 &= i\hat{P}_3 \\
\hat{Z}_4 &= i\left(\hat{P}_4 - \frac{1}{2}\hat{P}_2^2\right) \\
\hat{Z}_5 &= i\left(\hat{P}_5 - \frac{1}{2}\left(\hat{P}_2\hat{P}_3 + \hat{P}_3\hat{P}_2\right)\right).
\end{aligned} \tag{2.9}$$

Eq. (2.9), shows that if $\hat{Z}_1 = 0$, that is, if the perturbation is unbiased, the first two nonzero orders of the Magnus expansion equal the first nonzero orders of the Dyson expansion, except for a phase. Starting at fourth order, the terms for Dyson and Magnus expansion differ. This connection between Magnus and Dyson expansion is quite powerful, because, unlike the terms of the Magnus expansion, the terms of the Dyson expansion do not involve nested commutators. This avoids having to deal with commutators, and also avoids costly matrix multiplications when calculating the terms numerically. Nevertheless, both expansions require calculations of nested integrals. In the following sections, we calculate the Magnus expansion using Eq. (2.9), allowing us to efficiently and analytically track the role of different errors.

For analytical calculations, it might be relevant to keep in mind that even though Dyson and Magnus expansion have the same first terms if the first order is zero, the difference between the expansions lies not only in the mathematical expressions of each order, but also in the structure of the time evolution operator. While the Dyson expansion expresses the time evolution operator in terms of a power series, the Magnus expansion [Bla+98] provides an effective time-independent Hamiltonian, which captures the same dynamics as the original time-dependent Hamiltonian.

If $\hat{H}$ is bounded, then a sufficient convergence criterion for the Magnus expansion is [Bla+09]

$$\int_{t_0}^{t} \left\| -i\hat{H}(\tau) \right\| \mathrm{d}\tau < \pi. \tag{2.10}$$

Also we can set a bound on each order of the Magnus expansion

$$\left\|\hat{Z}_k\right\| \leq \pi \left(\frac{1}{\xi} \int_{t_0}^{t} \left\|-i\hat{H}(\tau)\right\|_2 \mathrm{d}\tau\right)^k, \tag{2.11}$$

with

$$\xi = \frac{1}{2} \int_0^{2\pi} \frac{1}{2 + \frac{x}{2}\left(1 - \cot\left(\frac{x}{2}\right)\right)} \mathrm{d}x \approx 1.0869. \tag{2.12}$$

Unfortunately, those convergence criteria are only sufficient criteria, whereas a necessary criterion does, to the authors' knowledge, not exist.

2.1.2. Perturbations to the driven harmonic oscillator

To underscore the existence of error mechanisms arising from low perturbation yet higher-order scattering processes under strong driving, we first show how they emerge under a generic driven Hamiltonian.

We consider a perturbative coupling between a coupler element, here harmonic oscillator (HO), and another (computational) subsystem. The systems are treated in an appropriate rotating frame or interaction picture. This encompasses the Hamiltonian of the Mølmer-Sørensen gate, but also coupling mechanisms for a wide variety of other fast two-qubit gates [Pai+16; HK21; LCM24; Bar+19; Rea+18; Neg+21; Sch+03b; Ben+08b; Sch+18; Meh+19; Cla+21; KCM22; Web+24] and readout [BGB10; Ree+10; Jer+24] mechanisms.

We start with generically expanding the interaction in orders of a small parameter λ,

$$\hat{H} = \hat{H}_0(t) + \lambda \hat{H}_1(t) + \mathcal{O}(\lambda^2), \tag{2.13}$$

which acts on the composite space $\mathcal{H}_{\mathrm{HO}} \otimes \mathcal{H}_{\mathrm{qubits}}$. Now, we consider the effect of different resonance offsets (ω_k) accompanying the different perturbation orders of the Hamiltonian ($\hat{H}_k$), or more precisely

$$\hat{H}_k(t) = \hbar\Omega(t)\hat{a}^k e^{-i\omega_k t} \otimes \hat{O}_k + H.c., \tag{2.14}$$

where Ω is the drive amplitude, which we cannot always assume is smaller than the resonance offsets ω_k due to strong driving, $\hat{O}_k$ are operators acting on the

qubit subspace, and $\hat{a}, \hat{a}^\dagger$ are the annihilation and creation operators, respectively. Note that we have fixed a common drive amplitude and specific powers of the harmonic oscillator operators, but this is simply done for concreteness and readability.

In the first-order Magnus expansion, we have $\hat{Z}_1 = \frac{1}{\hbar}\int_0^T dt\hat{H}(t)$ corresponding to oscillating (off-resonant) terms. Often these are enforced to integrate to zero, but not strictly needed for our purposes in this subsection.

The second order of the Magnus expansion is given by

$$\hat{Z}_2 = \frac{i}{2\hbar^2}\int_0^T dt \int_0^t d\tau \big[\hat{H}(t), \hat{H}(\tau)\big], \tag{2.15}$$

where the commutator can be broken down as

$$\begin{aligned}\big[\hat{H}(t), \hat{H}(\tau)\big] = \big[\hat{H}_0(t), \hat{H}_0(\tau)\big] + \lambda^2\big[\hat{H}_1(t), \hat{H}_1(\tau)\big] \\ + \lambda\big[\hat{H}_1(t), \hat{H}_0(\tau)\big] + \lambda\big[\hat{H}_0(t), \hat{H}_1(\tau)\big] + \dots\end{aligned} \tag{2.16}$$

The important point to note is that the first line of Eq. (2.16) corresponds to resonant driving while the second does not, since the zeroth and first-order frequency offsets are non-commensurate. In particular, in later sections the λ^2 term will correspond to the Mølmer-Sørensen gate interaction.

The third order of the Magnus expansion similarly contains a sum of commutators as in Eq. (2.7),

$$\big[\big[\hat{H}(t), \hat{H}(\tau)\big], \hat{H}(\tau')\big] + \big[\hat{H}(t), \big[\hat{H}(\tau), \hat{H}(\tau')\big]\big], \tag{2.17}$$

but which are always non-resonant, since there is an odd number of factors. Unlike in the first order, these are generally not calibrated to integrate to zero, but these errors will still be relatively small.

Meanwhile, going to the fourth order $\hat{Z}_4$, the Magnus expansion will introduce commutators of the form

$$\lambda^2\big[\big[\big[\hat{H}_0(t), \hat{H}_1(\tau)\big], \hat{H}_0(\tau')\big], \hat{H}_1(\tau'')\big], \tag{2.18}$$

and other permutations thereof, that is, where we have an even number of H_0

and H_1 factors.

We see that we have a resonant coupling interaction of the same perturbation order as the one arising from $\hat{Z}_2$. Because we drive relatively strongly, the fact that the interaction is fourth order in Ω does not in general suppress the transition.

The general takeaways are twofold: the first is that the perturbation order of the Hamiltonian need not be linked with increasing expansion orders when the driving itself is non-perturbative. This is especially true in many-level systems where spurious resonances may arise. The second takeaway is that the expansion is non-monotonic, for example, with the error increasing for the first four orders before eventually reducing again.

Therefore, in this general case, it is insufficient to terminate the series at low order. Fig. 2.1 shows the parameter scaling of errors in the Magnus expansion for the Mølmer-Sørensen gate Hamiltonian studied in this work, where $\lambda = \eta$ is the Lamb-Dicke factor.

Nonetheless, such higher-order processes must be carefully dealt with whenever coupler elements are driven strongly to accelerate entangling operations between subsystems.

2.1.3. Mølmer-Sørensen gate system Hamiltonian

We model the trapped-ion system as two qubits coupled to a harmonic oscillator [Win+98]. The Hamiltonian of the uncoupled two-qubit system is

$$\hat{H}_q = \hbar\omega_q \hat{J}_z \tag{2.19}$$

with qubit transition frequency ω_q and collective spin operator

$$\hat{J}_i = \frac{1}{2}\left(\mathbb{1} \otimes \hat{\sigma}_i + \hat{\sigma}_i \otimes \mathbb{1}\right), \tag{2.20}$$

where σ_i, $i = x, y, z$ are the Pauli operators. The modes of the ion motion are modeled as harmonic oscillators (see Section 1.2.3)

$$\hat{H}_{\text{motion}} = \hbar \sum_p \nu_p \hat{a}_p^\dagger \hat{a}_p \tag{2.21}$$

with frequency ν_p, and lowering and raising operator, $\hat{a}_p$ and $\hat{a}_p^\dagger$, of the pth eigenmode, respectively.

The interaction between the systems is invoked by a monochrome classical light field with drive envelope $\Omega(t)$ and wave number k along the trap axis. The entangling operation of the Mølmer-Sørensen gate is generated by driving two laser frequencies at the same time [SM00]. When each laser is detuned by a frequency $\pm\delta$ from the qubit frequency ω_q, the Hamiltonian total can be written as

$$\hat{H} = \hbar\omega_q \hat{J}_z + \hbar\nu\hat{a}^\dagger\hat{a} + 2\hbar\Omega(t)\sum_p \sum_{\mu=\pm1} \cos\left(k\hat{q}_p - (\omega_q + \mu\delta)t\right)\hat{J}_x, \tag{2.22}$$

where $\hat{q}_p = \sqrt{\frac{\hbar}{2M\nu_p}}\left(\hat{a}_p + \hat{a}_p^\dagger\right)$, with M the mass of a single ion, describes the position operator for the ions in the pth motional mode.

As described in Section 1.2.3, the motion of two ions can be separated into the center of mass mode and the breathing mode. Since the frequencies of those modes differ by a factor of $\sqrt{3}$, it can be legit to neglect all motional modes but one, as long as the drive detuning δ is close enough to the frequency $\nu_p = \nu$ of this mode.

Moving to an interaction picture with respect to both qubits and motional mode, the Hamiltonian can be written in the RWA as

$$\hat{H} = \hbar\Omega(t)\cos(\delta t)\left(\hat{J}_+ e^{ik\hat{q}(t)} + \hat{J}_- e^{-ik\hat{q}(t)}\right), \tag{2.23}$$

where $\hat{J}_\pm = \left(\hat{J}_x \pm i\hat{J}_y\right)$ are the collective spin raising and lowering operators. We describe the motional mode with $k\hat{q}(t) = \eta\left(\hat{a}e^{-i\nu t} + \hat{a}^\dagger e^{i\nu t}\right)$, where η is the Lamb-Dicke factor, which describes the qubit-trap coupling strength.

In the following sections, we need to calculate integrals of products of the Hamiltonian at different times. Therefore, it is useful to expand the Hamiltonian as a power series in the raising and lowering operators that act on the motional-mode subspaces. We first express the operator for the motional mode in terms of the creation and annihilation operators ($\hat{a}^\dagger$, $\hat{a}$). Then we use the Baker-Campbell-

Hausdorff (BCH) formula [Hal15] to factorize the operator exponentials as

$$e^{ik\hat{q}(t)} = e^{i\eta\left(\hat{a}e^{-i\nu t}+\hat{a}^\dagger e^{i\nu t}\right)} = e^{i\eta\hat{a}^\dagger e^{i\nu t}} e^{i\eta\hat{a}e^{-i\nu t}} e^{\frac{-\eta^2}{2}}. \tag{2.24}$$

Next, we expand both exponentials in Eq. (2.24) via Taylor series, introducing two counting indices for higher powers of raising and lowering operators. A change of variables ensures that the time-dependent part runs only over a single index m:

$$\begin{aligned} e^{ik\hat{q}(t)} &= e^{-\frac{\eta^2}{2}} \sum_{l=0}^{\infty}\sum_{k=0}^{\infty} \frac{(i\eta)^{l+k}}{l!k!} (\hat{a}^\dagger)^l (\hat{a})^k e^{i\nu(l+k)t} \\ &= e^{-\frac{\eta^2}{2}} \sum_{m=-k}^{\infty}\sum_{k=0}^{\infty} \frac{(i\eta)^{2m+k}}{(m+k)!k!} (\hat{a}^\dagger)^{m+k} (\hat{a})^k e^{i\nu m t} \end{aligned} \tag{2.25}$$

The sums implicate that $k \geq 0$ and $m \geq -k$, which corresponds to $m \in \mathbb{Z}$, $k \geq 0$, and $k \geq -m$. Thus, the terms in Eq. (2.25) can be grouped together with the index m for the sideband order (corresponding to the number of phonons created or annihilated) and Eq. (2.25) can be rewritten as

$$e^{ik\hat{q}(t)} = \sum_{m=-\infty}^{\infty} e^{i\nu m t} \hat{A}_m, \tag{2.26}$$

where we defined the mth sideband assisted transition operator

$$\hat{A}_m = e^{-\frac{1}{2}\eta^2} \sum_{k=\max(0,-m)}^{\infty} \frac{\eta^{2k+m} i^{2k+m}}{(m+k)!k!} (\hat{a}^\dagger)^{k+m} (\hat{a})^k \tag{2.27}$$

Using that $\left(\hat{A}_{-m}\right)^\dagger = (-1)^m \hat{A}_m$, one can show that the conjugate transpose of Eq. (2.26) can be expressed as

$$e^{-ik\hat{q}(t)} = \sum_m e^{i\nu m t} (-1)^m \hat{A}_m. \tag{2.28}$$

Inserting Eqs. (2.26) and (2.28) into Eq. (2.23) leads to the simplified Hamiltonian

$$\hat{H}(t) = \hbar\Omega(t) \sum_{m\in\mathbb{Z}} \sum_{\mu=\pm1} e^{i(m\nu+\mu\delta)t} \hat{J}_\mu \hat{A}_m, \tag{2.29}$$

where operations on the qubit subspace are described by the collective spin op-

erator,

$$\hat{J}_m = \frac{1}{2}\left(\hat{J}_+ + (-1)^m \hat{J}_-\right) = \begin{cases} \hat{J}_x & \text{if } m \text{ even} \\ i\hat{J}_y & \text{if } m \text{ odd} \end{cases}, \tag{2.30}$$

which acts on both qubits. The transition in the motional mode under absorption or emission of m phonons is given by the mth sideband assisted transition operator $\hat{A}_m$, defined in Eq. (2.27).

In the following sections, we calculate the Magnus expansion for the Hamiltonian Eq. (2.29) order by order, discussing the effect of each term on the effective Hamiltonian and gate fidelity, and discussing the conditions under which specific terms are suppressed.

2.2. Resonance conditions

The time-dependent part of the Hamiltonian that is given in Eq. (2.29) consists of exponential functions and so do the integrands in the Magnus expansion. Depending on the factor in the exponential and the bounds of the integrals, these integrals may rotate to zero. Regarding the Mølmer-Sørensen gate, our goal is to set conditions on how to suppress certain transitions, as depicted in Fig. 2.1, while controlling the electronic double-excitation transitions, which are required for the entangling gate. For this purpose, we associate the resonance conditions at time T with beat-note frequencies

$$N(m,\mu) := \underbrace{\frac{\nu T}{2\pi}}_{K} m + \underbrace{\frac{\delta T}{2\pi}}_{L} \mu, \tag{2.31}$$

with dimensionless gate duration K and dimensionless laser detuning frequency L. As before, m is the sideband order and μ is the detuning sign. For better readability, only the zeroth harmonic of the pulse ($\Omega(t) = \Omega$) is included in this section. The general formulas for time-dependent drive amplitudes are provided in Section 2.2.5. Using the notation for the beat-note frequencies, the Hamiltonian

Eq. (2.29) takes the simplified form

$$\hat{H}(t) = \hbar\Omega \sum_{m=-\infty}^{\infty} \sum_{\mu=\pm 1} e^{i\frac{2\pi}{T}N(m,\mu)t} \hat{J}_m \hat{A}_m. \tag{2.32}$$

The Magnus expansion can be very cumbersome to calculate beyond second order. In the following sections, we benefit from the relation between Dyson and Magnus expansion, given in Eq. (2.8). In effect, this means that calculation of the kth order Magnus expansion terms can be reduced in its time dependence to solving nested integrals of the form

$$I_{N_1,\cdots,N_k} = \int_0^T \mathrm{d}t_k \int_0^{t_k} \mathrm{d}t_{k-1} \cdots \int_0^{t_2} \mathrm{d}t_1 e^{i\frac{2\pi}{T}\sum_{j=1}^{k} N_j t_j}, \tag{2.33}$$

where the exponent consists of the sum of the exponents of Eq. (2.32) evaluated at different times t_j and for different combinations of the beat-note frequencies $N_j \equiv N(m_j, \mu_j)$. Finding appropriate solutions to the conditions allows us then to significantly simplify the time-ordered operators in Eq. (2.3), rewritten here as

$$\hat{P}_k(t) = \left(-\frac{i\Omega}{\hbar}\right)^k \sum_{\substack{m_1\in\mathbb{Z}\\ \mu_1=\pm 1}} \cdots \sum_{\substack{m_k\in\mathbb{Z}\\ \mu_k=\pm 1}} \left(\hat{J}_{m_1}\hat{A}_{m_1}\right)\cdots\left(\hat{J}_{m_k}\hat{A}_{m_k}\right) I_{N_1\cdots N_k}, \tag{2.34}$$

which factors out the time dependence.

We proceed to calculate the leading orders of the nested integrals analytically and then verify their accuracy numerically. A main challenge is to ascertain whether for single coefficients N_j the integrals are zero, and whether they combine to sum up to zero, each corresponding to different resonance conditions.

In general, nested integrals of the form

$$I_{N_k,N_{k-1},\cdots,N_1}(t,b) = \int_0^t \mathrm{d}t_k \int_0^{t_k} \mathrm{d}t_{k-1} \cdots \int_0^{t_2} \mathrm{d}t_1 e^{b\sum_{j=1}^{k} N_j t_j} \tag{2.35}$$

can be hard to calculate, especially for fast oscillating numerics, because the value of the integral depends on whether single coefficients N_j are zero, or whether they sum up to zero, as can be seen in Eqs. (2.41) and (2.44).

The integrals can however be simplified using integration by parts. The analytical forms and their numerical evaluation can then be calculated using the SymPy [Meu+17] and NumPy [Har+20] python packages, respectively. A pseudocode example for the calculation can be found in Section A.

2.2.1. First-order condition

The resonance condition for the first Magnus order results from the integral I_N, which produces $\hat{Z}_1 = i\hat{P}_1$ given by

$$\hat{Z}_1 = \Omega \sum_{m=0}^{\infty} \sum_{\mu=\pm 1} \underbrace{\frac{e^{i(m\nu+\mu\delta)T} - 1}{i\,(m\nu + \mu\delta)}}_{\text{resonance term}} \hat{J}_m \hat{A}_m. \tag{2.36}$$

This term describes the phonon-assisted flipping of the qubits. For the entangling gate, we want to suppress single-qubit flips at the final time T, hence we tune the parameters such that $\hat{Z}_1 = 0$. A straightforward solution is to set all the resonance terms to zero, which requires the beat-note frequency to be a nonzero integer

$$N(m, \mu) \in \mathbb{Z}^*, \tag{2.37}$$

which implies that also K and L are integers. In the case of a constant drive amplitude, fulfilling Eq. (2.37) can be ensured with a laser detuning δ, which is not a multiple of the motional mode frequency ν. Note that due to strong driving (compared to the detuning), the motional mode will nonetheless be excited, and only at the final time does it revert to zero. If, on the other hand, the laser detuning is on resonance with the motional mode frequency $\delta = \nu$, the sideband transition remains populated also at the final time [Win+98]. Small detuning of the laser frequency from the sideband violates Eq. (2.37) and thus leads to errors in $\hat{Z}_1$ [Mar+22], but is beyond the scope of this work.

2.2.2. Second-order condition

If the parameters are chosen such that the first order of the Magnus expansion is suppressed, $\hat{Z}_1 = 0$, the second order of the Magnus expansion equals the second order of the Dyson expansion: $\hat{Z}_2 = i\hat{P}_2$, as shown in Eq. (2.9). Inserting

the Hamiltonian in Eq. (2.32) into Eq. (2.7) yields

$$\hat{Z}_2 = i\Omega^2 \sum_{m_1,m_2=0}^{\infty} \sum_{\mu_1,\mu_2=\pm 1} \hat{J}_{m_1}\hat{J}_{m_2}\hat{A}_{m_1}\hat{A}_{m_2} I_{N_1,N_2}, \tag{2.38}$$

with the resonance integral

$$I_{N_1,N_2} = \int_0^T e^{i\frac{2\pi}{T}N_1 t}\mathrm{d}t \int_0^t e^{i\frac{2\pi}{T}N_2 \tau}\mathrm{d}\tau\,, \tag{2.39}$$

given by Eq. (2.33), where the beat-note frequencies are now defined as

$$N_j(m_j,\mu_j) = m_j K + \mu_j L. \tag{2.40}$$

We focus on the case, where $N_j \in \mathbb{Z}\ \forall j$. Then, the non-vanishing contributions to the integral are:

$$I_{N_1,N_2} = \begin{cases} \frac{T^2}{2} & N_1 = 0, N_2 = 0 \\ \frac{iT^2}{2\pi N_2} & N_1 = 0, N_2 \neq 0 \\ -\frac{iT^2}{2\pi N_1} & N_1 \neq 0, N_2 = 0 \\ -\frac{iT^2}{2\pi N_2} & N_1 \neq 0, N_2 \neq 0, N_1 + N_2 = 0 \end{cases} \tag{2.41}$$

Here, we have four resonance conditions. The first three conditions, where at least one $N_j = 0$, are the resonance conditions for the unwanted single-photon transitions. The fourth condition, where $N_j \neq 0$ and $N_1 + N_2 = 0$, is the resonance condition for a two-photon transition. This is what creates the desired entanglement for the Mølmer-Sørensen gate.

The expression for the second order of the Magnus expansion Eq. (2.38) can be simplified further given that single-photon transitions are suppressed ($\hat{Z}_1 = 0$). Assuming that the detuning δ of the laser from the qubit frequency is of the order of the trap frequency ν, which is required in any case to make sure that only a single motional mode is excited, then the two-photon resonance condition can be rewritten as

$$N_1 + N_2 = 0 \iff (m_1 = -m_2) \wedge (\mu_1 = -\mu_2). \tag{2.42}$$

In Section 2.2.4, we discuss the conditions for the validity of Eq. (2.42) in more detail.

The simplification Eq. (2.42) allows rewriting the second-order Magnus term in Eq. (2.38) as

$$\begin{aligned} Z_2 &= -i\frac{\Omega^2}{\hbar^2}\sum_{m\in\mathbb{Z}}\sum_{\mu=\pm1}\hat{J}_m^2\hat{A}_m\hat{A}_{-m}\frac{-iT^2}{2\pi}\underbrace{\left(\frac{1}{mK+\mu L}+\frac{1}{mK-\mu L}\right)}_{\frac{2mK}{mK+\mu L}} \\ &= \frac{-\Omega^2T^2}{\pi\hbar^2}\sum_{m=1}^{\infty}\sum_{\mu=\pm1}\hat{J}_m^2\left[\hat{A}_m,\hat{A}_{-m}\right]\frac{mK}{mK+\mu L}. \end{aligned} \tag{2.43}$$

Note that $\left[\hat{A}_m,\hat{A}_{-m}\right]$ is diagonal in the motional-mode subspace, because the matrix elements $\langle n'|\hat{A}_{m_1}\hat{A}_{m_2}|n\rangle$ are only nonzero if $n'-n=m_1+m_2$. Thus, $\hat{Z}_2$ is diagonal in the motional-mode subspace as well. Therefore, as can be seen from Fig. 2.1, the terms in $\hat{Z}_2$ create simultaneous flips on the qubits. However, these conditions alone do not ensure that the Hamiltonian generates the correct gate. As we discuss next in Section 2.3, recalibrating the weights of these and other terms affects the rotation angle about the $\hat{J}_x^2$ and $\hat{J}_y^2$ operators.

2.2.3. Higher-order conditions

When $\hat{Z}_1=0$, the third order of the Magnus expansion simplifies to $\hat{Z}_3=i\hat{P}_3$. Computing this term involves calculation of a triple integral. Assuming that we suppress single-photon transitions ($N_j\in\mathbb{Z}^*\ \forall j$), the resonance integral of third order is

$$I_{N_1,N_2,N_3}=\frac{T^3}{4\pi^2N_3}\left(\frac{\delta_{N_1+N_2}}{N_2}+\frac{\delta_{N_2+N_3}}{N_1}\right). \tag{2.44}$$

This integral is zero unless $N_1+N_2=0$ or $N_2+N_3=0$, which are thus the resonance conditions for the third order transitions. Because of the complexity of Eq. (2.44), there is no compact form for $\hat{Z}_3$ beyond Eq. (2.34), such as we have derived for $\hat{Z}_2$ in Eq. (2.43). The same applies for $\hat{Z}_4$ and $\hat{Z}_5$, but we provide the leading analytical error terms for $\hat{Z}_3$ and $\hat{Z}_4$, for the typical case of a rectangular pulse in Section 2.3.2. We then evaluate numerically the significance of those

terms in Section 2.3.3.

2.2.4. Suppression of trivial resonances

The terms in Table 2.1 were calculated using computer algebra tools, assuming that the detuning of the laser avoids certain sideband ranges, which is justified as follows. In order to simplify the expression for $\hat{Z}_2$, we have assumed in Eq. (2.42) that

$$N_1 + N_2 = 0 \iff (m_1 + m_2 = 0) \wedge (\mu_1 + \mu_2 = 0) \tag{2.45}$$

To drive a single motional mode only, the laser detuning must be close to the motional mode frequency $K - L \ll K$. If $\mu_1 + \mu_2 \neq 0$, then this condition can be rewritten using the resonance condition $N_1 + N_2 = 0$:

$$1 + \frac{m_1 + m_2}{\mu_1 + \mu_2} = \frac{K - L}{K} \ll 1. \tag{2.46}$$

Checking the condition for the allowed values of $\mu_1 + \mu_2$ yields:

1. $1 - \frac{m_1+m_2}{2} \ll 1$ for $\mu_1 + \mu_2 = -2$. This can only be fulfilled for $m_1 + m_2 = 1$ and yields the resonance condition $K = 2L$.
2. $1 - (m_1 + m_2) \ll 1$, which does not yield a result for integer m_1, m_2.
3. Nor does $1 + (m_1 + m_2) \ll 1$.
4. $1 + \frac{m_1+m_2}{2} \ll 1$ can be fulfilled for $m_1 + m_2 = -1$ and yields the resonance condition $K = 2L$.

Thus, as long as $K - L \ll K$ and specifically $K \neq 2L$, condition Eq. (2.42) remains valid.

One can make similar assumptions for the higher orders of the Magnus expansion. If the expressions in Table 2.1 were completely general, they would contain explicit case distinctions for certain resonances, which would make the table even more unwieldy. Hence, in order to keep the expressions in Table 2.1 simple and concise, we explicitly ignore those results with $jK = lL$ at the kth order of the Magnus expansion, as long as one of the following conditions on $\frac{l-j}{l} = \frac{K-L}{K}$ is true:

1. $\frac{l-j}{l} \leq 0$, which does not appear in experiment by construction, because we defined $K > 0$ and $K - L > 0$.
2. $\frac{l-j}{l} \geq \frac{1}{km_{\max}}$, where $m_{\max}$ is the maximum value of m which is included in the calculation of the Magnus expansion (for our calculations $m_{\max} = 3$).

However, since the first condition is by construction never met and since the second condition is false in most cases as long as $\frac{K-L}{K} \ll 1$, exclusion of these trivial resonances is mostly a formal step to avoid lengthy case distinctions of unrealistic terms in Table 2.1. Still, if $\frac{K-L}{K}$ is approaching 1, in order to assure the validity of the terms in Table 2.1. one has to make sure that there is no $j \leq km_{\max}$ and $|l| \leq k$ such that $jK = lL$ (which is fine for $K = 28$ and $K - L = 3$, as an example). Otherwise, there may be additional terms that must be taken into account.

2.2.5. Generalization to shaped pulses

We can extend the calculations in the previous section easily to shaped pulses.

We Fourier-decompose the time-dependent parts in Eq. (2.23) and write the drive amplitude over the time interval $[0, T]$ as a Fourier series

$$\Omega(t) = \Omega \sum_{M \in \mathbb{Z}} c_M e^{i\frac{2\pi}{T}Mt}, \tag{2.47}$$

with $c_{-M} = c_M^*$, and where in principle we truncate the series at a small frequency for bandwidth considerations. The Hamiltonian can hence be written as

$$\hat{H}(t) = \hbar\Omega \sum_{M,m \in \mathbb{Z}} \sum_{\mu = \pm 1} c_M e^{i\frac{2\pi}{T}N(M,m,\mu)t} \hat{J}_m \hat{A}_m, \tag{2.48}$$

where the beat-note frequency is now defined as

$$N(M, m, \mu) := M + \underbrace{\frac{\nu T}{2\pi}}_{K} m + \underbrace{\frac{\delta T}{2\pi}}_{L} \mu. \tag{2.49}$$

In order to suppress the first order of the Magnus expansion, we now need to take into account corrections to the beat-note frequency induced by the additional

term due to the pulse shape.

The corrections to the beat-note frequency modify the time-dependent part of the effective Hamiltonian, which in turn changes the amplitude of the single error contributions. However, they do not affect the structure or the properties of the operators.

First-order condition

The general expression for the first order of the Magnus expansion with time-dependent drive amplitude is

$$\hat{Z}_1 = \Omega \sum_{M,m=-\infty}^{\infty} \sum_{\mu=\pm 1} c_M \underbrace{T \frac{e^{i\frac{2\pi}{T}N(M,m,\mu)} - 1}{2\pi i N(M,m,\mu)}}_{\text{resonance condition}} \hat{J}_m \hat{A}_m. \tag{2.50}$$

As in the previous section, in order to ensure $\hat{Z}_1 = 0$, the beat-note frequency must be a nonzero integer: $M + mK + \mu L \neq 0 \; \forall M, m, \mu$. This implies for instance that $K - L \neq M$, setting additional conditions for the choice of K and L.

Second-order condition

The second order of the Magnus expansion for time-dependent drive amplitudes is

$$\hat{Z}_2 = i\Omega^2 \sum_{\substack{M_1,M_2=0 \\ m_1,m_2=0}}^{\infty} \sum_{\mu_1,\mu_2=\pm 1} c_{M_1} c_{M_2} \hat{J}_{m_1} \hat{J}_{m_2} \hat{A}_{m_1} \hat{A}_{m_2} I_{N_1,N_2}, \tag{2.51}$$

where the beat-note frequencies in the resonance integral of second order I_{N_1,N_2} are now defined as

$$N_j = M_j + m_j K + \mu_j L. \tag{2.52}$$

The resonance integral takes the same values as described in Eq. (2.41). The expression for the second order of the Magnus expansion in Eq. (2.51) can be simplified further if the two-photon resonance condition

$$\begin{aligned} & M_1 + m_1 K + \mu_1 L + M_2 + m_2 K + \mu_2 L = 0 \\ \iff & (M_1 = -M_2) \wedge (m_1 = -m_2) \wedge (\mu_1 = -\mu_2) \end{aligned} \tag{2.53}$$

is satisfied.

Trivial resonance conditions

For a rectangular pulse $\Omega(t) = \Omega$, the multipartite resonance condition Eq. (2.53) is valid if the laser detuning is itself only slightly detuned from the motional mode frequency: $\frac{K-L}{K} \ll 1$, see Section 2.2.4. For a non-rectangular pulse however, the exact conditions are more complex. To keep the resulting analytic expressions simple and concise, our results for shaped pulses do not include terms that satisfy

$$j_1 K + j_2 L + j_3 \neq 0 \tag{2.54}$$

for the kth Magnus order with maximal sideband order $m_{\max}$, where the integers j_i fulfill $0 \leq |j_1| \leq k m_{\max}$, $|j_2| \leq k$, and $|j_3| \leq \max(M)k$. Compared to rectangular drive pulses, the number of trivial resonances that are excluded explicitly is significantly larger, as the whole calculations of the Magnus terms for shaped pulses requires computation of more terms and thus more calculation capacities. The higher complexity of these resonance conditions requires more caution for the choice of parameters. So is for example $K - L \neq 2$ a trivial condition, which should be avoided, for a $\sin^2$ pulse, since $\max(M) = 2$.

2.3. Error terms for rectangular drive pulses

In this section, we present the leading order terms of the Magnus expansion in the Lamb-Dicke parameter η for the Mølmer-Sørensen gate, driven with rectangular pulses, and we examine the impact of each error term on the fidelity. Furthermore, we use analytical expressions for the fidelity, using the Magnus expansion to different orders, to calculate optimized expressions for the drive amplitude.

2.3.1. Choice of fidelity

The Bell state fidelity, for an initial state ρ_0 and a target qubit state $|\psi_{\text{target}}\rangle$, defined as

$$\mathcal{F}_{\text{Bell}} = \langle \psi_{\text{target}} | \text{Tr}_{\text{motion}}\{\hat{U}(T)\rho_0\hat{U}^\dagger(T)\} | \psi_{\text{target}} \rangle \tag{2.55}$$

is often used in experiments [SM00; Meh+20; Meh+19; Cla+21; Bal+16; Tin+21; Gae+16] and therefore allows for straightforward comparison. The main advantage of this metric is that it is a good measure of (maximally) achievable entanglement, while at the same time not taking into account relative phases which, if necessary, can be corrected, for example with single qubit gates. Also, the Bell state fidelity allows for straightforward calculation of the fidelity for Hamiltonians of the form

$$\sum_n \sum_{j=x,y,z} \left(d_j^{(n)} \hat{f}_j^2 \right) \otimes |n\rangle\langle n| \,, \tag{2.56}$$

which corresponds, as we describe in Section 2.3.2, in leading order to the effective Hamiltonian for the Mølmer-Sørensen gate. Since $\hat{f}_x^2$ and $\hat{f}_y^2$ are qubit entangling operators, and $\hat{f}_z$ only affects the phase of the collective qubit state, Eq. (2.56) describes an entangling operation on the qubits while leaving the of the motional mode unaltered. The Bell state fidelity of a Hamiltonian of the form Eq. (2.56) yields, considering an initial qubit state $|\psi_0\rangle = |00\rangle$, an entangled qubit target state $|\psi_t\rangle = \frac{1}{\sqrt{2}} \left(|00\rangle + e^{i\varphi} |11\rangle \right)$, and an initial motional mode state $\sum_{n=0}^{\infty} P_n |n\rangle\langle n|$, where P_n is the initial probability for the motional mode to be in state $|n\rangle$,

$$\mathcal{F}_{\text{Bell}} = \frac{1}{2} \left(1 - \sum_n P_n \sin(\varphi) \sin\left(d_x^{(n)} - d_y^{(n)} \right) \right). \tag{2.57}$$

Hence, considering a target state $|\psi_t\rangle = \frac{1}{\sqrt{2}} \left(|00\rangle - i |11\rangle \right)$ with a rotation angle $\varphi = -\frac{\pi}{2}$, the optimal fidelity $\mathcal{F}_{\text{Bell}} = 1$ is obtained if

$$\sum_n P_n \sin\left(d_x^{(n)} - d_y^{(n)} \right) = 1 \tag{2.58}$$

is fulfilled. This equation can be solved numerically, but to achieve an analytical solution, further approximations are necessary. Assume, P_n decays quickly with n, for example if P_n follows a thermal distribution $P_n = \frac{(\bar{n})^n}{(\bar{n}+1)^{n+1}}$ with small average phonon number $\bar{n} \ll 1$. In this case, the terms for $n > 0$ in Eq. (2.58) can be neglected, and the condition for optimal fidelity becomes $\sin\left(d_x^{(0)} - d_y^{(0)} \right) = 1$, and thus

$$d_x^{(0)} - d_y^{(0)} = \frac{\pi}{2}. \tag{2.59}$$

This equation is valid for the leading terms of the effective Hamiltonian for the Mølmer-Sørensen gate.

A drawback of the Bell state fidelity is that it requires specification of initial and target states. However, there are other measures which allow quantification of the fidelity in quantum computing without need for these requirements. One of those is the average (gate-overlap) fidelity, defined as

$$\mathcal{F}_{\text{av}} = \frac{1}{4}\left|\text{Tr}_{\text{qubits}}\left\{\sum_{n=0}^{\infty} P_n \langle n|\hat{U}(T)\hat{U}_{\text{target}}^{\dagger}|n\rangle\right\}\right|, \tag{2.60}$$

which requires specification of a target unitary $\hat{U}_{\text{target}} = \exp(i\phi\hat{J}_y^2)$. For the Mølmer-Sørensen gate, the angle is $\phi = \frac{\pi}{2}$.

The average fidelity yields nearly the same results as the Bell fidelity if the trace over the motional modes is weighted by the Boltzmann distribution, $P_n = \frac{\bar{n}^n}{(\bar{n}+1)^{n+1}}$ ensuring that performance is measured accordingly for more likely initial states. It is a more standard measure for quantum information settings [Ber+17], because it measures how close a gate is to the target gate, which is useful for implementation of quantum algorithms, where exact specification of the gate is reasonable.

Comparison of the target propagator and the effective Hamiltonian of the form Eq. (2.56) shows that retrieving a simplified expression for the coefficients at optimal fidelity, requires negligible values of d_x and d_z, and additionally

$$d_y = -\frac{\pi}{2}. \tag{2.61}$$

So, for a Hamiltonian of the form Eq. (2.56), if all terms but those proportional to $\hat{J}_y^2$ are negligible, the average fidelity yields a straightforward result. However, to calculate the impact of the $\hat{J}_x^2$- and $\hat{J}_z^2$-term as well, the Bell fidelity is more suitable, since Eq. (2.57) is a concise expression containing both d_x and d_y.

Another measure which could be taken into account is the *concurrence* C, which we defined in Eq. (1.8). It measures the amount of entanglement of the two-qubit state (see Section 1.1.2) and thus can give insight into the impact of the gate. Yet, the concurrence is more impractical for quantum computing applications,

because it is neither sensitive to the exact target state, nor to a specific target unitary.

2.3.2. Analytical expressions

In this section, we calculate the analytical expressions for the terms of the Magnus expansion one by one, by solving the time-ordered Dyson integrals for small sideband orders $|m|$. Moreover, for the leading order terms, which we show to be diagonal in the motional-mode subspace and to be of the form Eq. (2.56), we can also derive analytical expressions for the fidelity (see Section 2.3.1) and solve them with respect to Ω for optimal fidelity.

Errors and optimal drive amplitude at $\hat{Z}_2$

In Section 2.2.2 and in particular with Eq. (2.43) we have shown that the second order of the Magnus expansion can be written as

$$Z_2 = \frac{-\Omega^2 T^2}{\pi\hbar^2} \sum_{m=1}^{\infty} \sum_{\mu=\pm 1} \hat{J}_m^2 \left[\hat{A}_m, \hat{A}_{-m}\right] \frac{mK}{mK + \mu L}. \tag{2.62}$$

Evaluation of the commutator $\left[\hat{A}_m, \hat{A}_{-m}\right]$ shows that $\hat{Z}_2$ can be expressed in the form

$$\hat{Z}_2 = \sum_{n=0}^{\infty} \left(d_x^{(n)} \hat{J}_x^2 + d_y^{(n)} \hat{J}_y^2 \right) \otimes |n\rangle\langle n| \,, \tag{2.63}$$

with the standard form factors [SM00] that are the sum over even m for d_x and over odd m for d_y,

$$\begin{aligned} d_{x,y}^{(n)} = \mp \frac{\Omega^2 T^2}{2\pi} e^{-\eta^2} \sum_{m \text{ even, odd}} \sum_{M\mu} \frac{|c_M|^2}{M + mK + \mu L} (-\eta^2)^{|m|} \\ \left(L_{\min(n, n-m)}^{|m|}(\eta^2) \right)^2 \frac{\min(n, n-m)!}{\max(n, n-m)!}, \end{aligned} \tag{2.64}$$

where $L_a^{(b)}$ is the associated Laguerre polynomial [Win+98], with the additional condition that $L_a^{(b)} = 0$ if $a < b$.

In first order in the Lamb-Dicke coefficient η, the propagator is diagonal in the

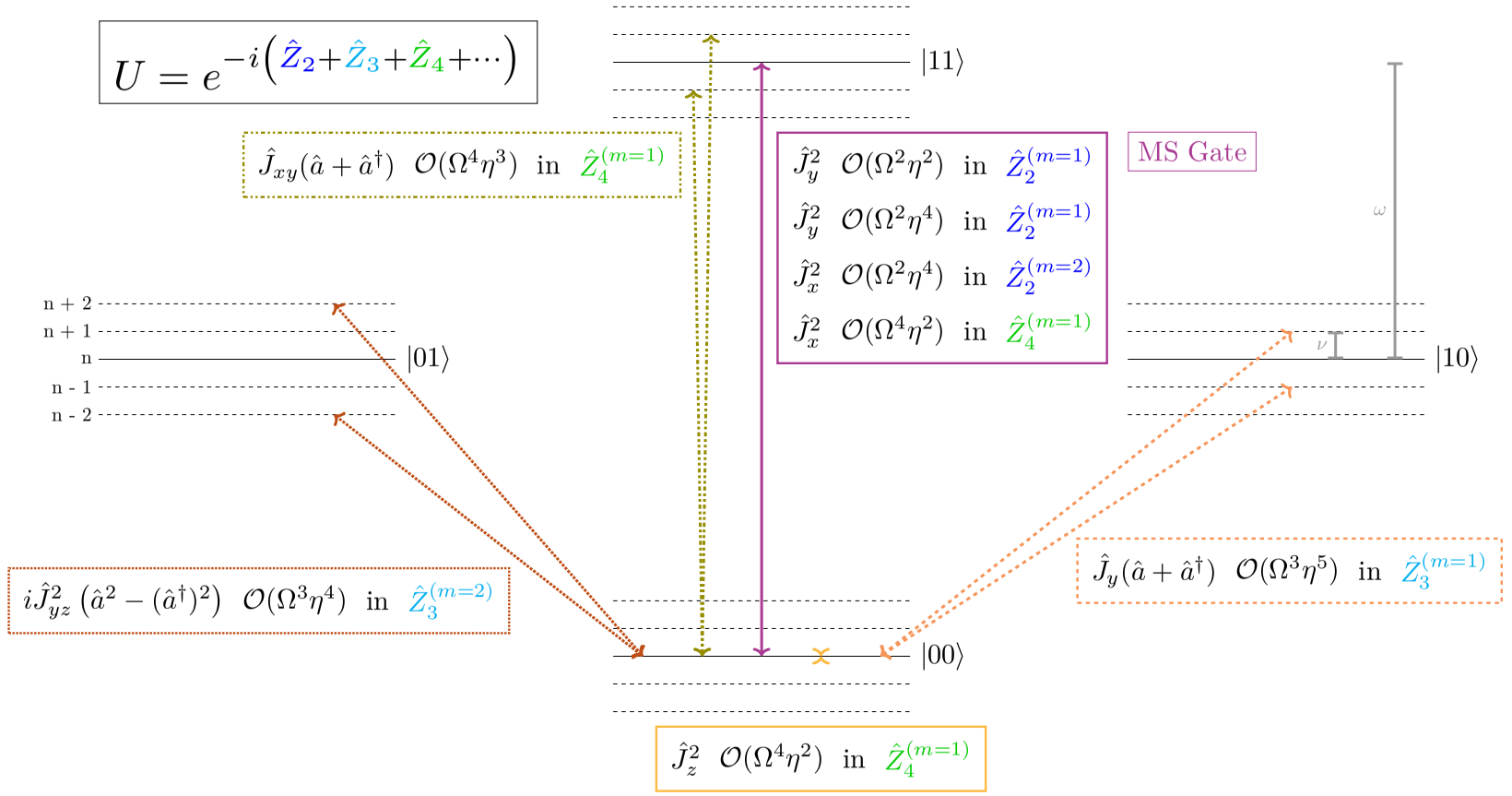

Figure 2.1.: Energy level diagram for the system in the interaction picture, with transitions connected to the $|00\rangle$ state being shown. The straight black lines depict the energy of the collective qubit states, and the dashed black lines depict contributions from the coupled qubit and motional mode states. The solid pink arrow between $|00\rangle$ and $|11\rangle$ shows the transitions which create the entangling gate. Those errors can be corrected by adjusting the drive amplitude. The dashed-dotted green arrows, left to the solid pink arrow, show sideband transitions that create an entangling operation in the qubit subspace, but additionally cause leakage into different motional mode states. The term proportional to $\hat{J}_z^2$ (yellow, at $|00\rangle$) only adds a phase to the collective qubit state. The dashed orange lines on the right-hand side denote first-sideband ($m = 1$) off-resonant error terms, and the dotted red lines on the left-hand side denote the second-sideband ($m = 2$) off-resonant error terms. Those terms can be minimized by time-shaping the drive amplitude. The full analytic expressions for the terms are listed in Table 2.1. The displayed lines denoting the transitions are just a sketch to give an intuition on the impact of each term, so not all potential transitions are shown.

Error	Operator	Term	Term at Ω_{LD}	Term at Ω_4	Order at Ω_4
Gate	$\hat{J}_y^2$	$-\frac{K\Omega^2T^2\eta^2}{\pi(K^2-L^2)}$	$-\frac{\pi}{2}$	$-\frac{\sqrt{2K}\pi L\eta\left(s-\sqrt{s^2-(K^2-L^2)}\right)}{(K^2-L^2)}$	$\mathcal{O}(\eta)$
$\hat{Z}_2^{(m=1)}$	$\hat{J}_y^2$	$\frac{K\Omega^2T^2\eta^4(2n+1)}{\pi(K^2-L^2)}$	$\frac{\pi\eta^2(1+2n)}{2}$	$\frac{\sqrt{2K}\pi L\eta^3(2n+1)\left(s-\sqrt{s^2-(K^2-L^2)}\right)}{(K^2-L^2)}$	$\mathcal{O}(\eta^3)$
$\hat{Z}_2^{(m=2)}$	$\hat{J}_x^2$	$-\frac{K\Omega^2T^2\eta^4(2n+1)}{\pi(4K^2-L^2)}$	$-\frac{\pi\eta^2\left(K^2-L^2\right)(2n+1)}{2(4K^2-L^2)}$	$-\frac{\sqrt{2K}\pi L\eta^3(2n+1)\left(s-\sqrt{s^2-(K^2-L^2)}\right)}{4K^2-L^2}$	$\mathcal{O}(\eta^3)$
$\hat{Z}_3^{(m=1)}$	$\hat{J}_y(\hat{a}+\hat{a}^\dagger)$	$-\frac{2K^2\Omega^3T^3\eta^5}{\pi^2(K^2-L^2)^2}$	$-\pi\eta^2\sqrt{\frac{K}{2(K^2-L^2)}}$	$-\frac{2^{\frac{7}{4}}\pi K^{\frac{5}{4}}L^{\frac{3}{2}}\eta^{\frac{7}{2}}\left(s-\sqrt{-K^2+L^2+s^2}\right)^{\frac{3}{2}}}{(K^2-L^2)^2}$	$\mathcal{O}(\eta^{\frac{7}{2}})$
$\hat{Z}_3^{(m=2)}$	$\hat{J}_x\left(\mathbb{1}-\hat{J}_y^2\right)(\hat{a}^2-\hat{a}^{\dagger 2})$	$\frac{K^2\Omega^3T^3\eta^4}{\pi^2(4K^2-L^2)(K^2-L^2)}$	$\frac{\pi\eta}{2}\sqrt{\frac{K}{2(K^2-L^2)(4K^2-L^2)}}$	$-\frac{2^{\frac{3}{4}}\pi K^{\frac{5}{4}}L^{\frac{3}{2}}\eta^{\frac{5}{2}}\left(s-\sqrt{s^2-(K^2-L^2)}\right)^{\frac{3}{2}}}{(4K^2-L^2)(K^2-L^2)}$	$\mathcal{O}(\eta^{\frac{5}{2}})$
$\hat{Z}_4^{(m=1)}$	$\hat{J}_{xy}(\hat{a}+\hat{a}^\dagger)$	$\frac{K\Omega^4T^4\eta^3}{\pi^3(K^2-4L^2)(K^2-L^2)}$	$\frac{\pi\left(K^2-L^2\right)}{4K\eta(K^2-4L^2)}$	$\frac{2\pi L^2\eta\left(s-\sqrt{s^2-(K^2-L^2)}\right)^2}{(K^2-L^2)(K^2-4L^4)}$	$\mathcal{O}(\eta)$
	$\hat{J}_z^2$	$-\frac{3K\Omega^4T^4\eta^2}{4\pi^3(4K^2-L^2)(K^2-L^2)}$	$-\frac{3\pi\left(K^2-L^2\right)}{16K\eta^2(K^2-4L^2)}$	$-\frac{3\pi L^2}{2(K^2-4L^2)}$	$\mathcal{O}(1)$
	$\hat{J}_y^2$	$\frac{K\Omega^4T^4\eta^2}{4\pi^3L^2(K^2-L^2)}$	$\frac{\pi\left(K^2-L^2\right)}{16KL^2\eta^2}$	$-\frac{\pi}{2}+\frac{\pi s\left(s-\sqrt{s^2-(K^2-L^2)}\right)}{(K^2-L^2)}$	$\mathcal{O}(1)$

Table 2.1.: Error terms for rectangular pulses. The second column shows the operator part of the term. The third to fifth column show the prefactor of the operator. The fourth and fifth column are the same as the third, except that the drive amplitude is set to $\Omega = \Omega_{\mathrm{LD}}$, defined in Eq. (2.67), and to $\Omega = \Omega_4$, defined in Eq. (2.77), respectively, with $s = \sqrt{2K}L\eta(1-\eta^2)$). The sixth column shows explicitly the order of the term of the fifth row.

motional mode subspace. Moreover, it is independent of the average motional mode population $\bar{n}$. So, neglecting the third and higher orders of the Magnus expansion, and to the lowest order of the Lamb-Dicke expansion, the given system produces a temperature-independent entangling operation on the qubits, while not affecting the state of the motional mode.

The form factors d_x and d_y, given in Eq. (2.64), are $\mathcal{O}(\eta^{2|m|})$ at sideband order $|m|$. Thus, for $\eta < 1$, it is sufficient to consider the first two sideband orders, unless the terms are expanded up to the sixth order in η or further. In the first and second sideband order $|m| \leq 2$, the form factors become

$$\begin{aligned} d_x^{(n)} &= -\frac{\Omega^2 T^2}{\pi} \frac{K}{(4K^2 - L^2)} (2n+1)\eta^4 + \mathcal{O}(\eta^6 n^2) \\ d_y^{(n)} &= \frac{\Omega^2 T^2}{\pi} \frac{K}{(K^2 - L^2)} \left((2n+1)\eta^4 - \eta^2 \right) + \mathcal{O}(\eta^6 n^2). \end{aligned} \tag{2.65}$$

To the first nonzero order of η, taking $k = 0$ and the first sideband order $|m| = 1$, the form factors in Eq. (2.65) simplify, such that $d_x^{(0)} = 0$ and the second order Magnus term equals to

$$\hat{Z}_2 = d_y^{(0)} \hat{J}_y^2 = -\frac{\Omega^2 T^2}{\pi} \frac{K}{K^2 - L^2} \eta^2 \hat{J}_y^2. \tag{2.66}$$

The optimal parameters fulfill a $\frac{\pi}{2}$-rotation around $\hat{J}_y^2$ yielding an equation (c.f. Eq. (2.61)) that can straightforwardly be solved, leaving us with

$$\Omega_{\mathrm{LD}} = \frac{\pi}{T\eta} \frac{\sqrt{(K^2 - L^2)}}{\sqrt{2K}}, \tag{2.67}$$

where we assume that the motional mode is initially in the vacuum state $\bar{n} = 0$.

Taking the next order of the Lamb-Dicke expansion into account gives the Lamb-Dicke error term

$$\hat{Z}_2^{(m=1)} = \frac{iK\Omega^2 T^2 \eta^4 (2n+1)}{\pi (K^2 - L^2)} \hat{J}_y^2 = \hat{J}_y^2 \mathcal{O}(\Omega^2 \eta^4), \tag{2.68}$$

which corresponds to the second row in Table 2.1. Taking additionally the next sideband order into account, with $|m| = 2$, gives the sideband error term (third

row in Table 2.1)

$$\hat{Z}_2^{(m=2)} = -\frac{iK\Omega^2 T^2 \eta^4}{\pi\,(4K^2 - L^2)}(2n+1)\hat{J}_x^2 = \hat{J}_x^2 \mathcal{O}(\Omega^2\eta^4). \tag{2.69}$$

Both errors have already been studied in the original work, Ref. [SM00], and can be minimized by further adjusting the drive amplitude

$$\Omega_2 = \frac{\pi}{T\eta}\sqrt{\frac{(K^2 - L^2)(4K^2 - L^2)}{2K\left(\eta^2(2L^2 - 5K^2) + (4K^2 - L^2)\right)}}, \tag{2.70}$$

which can be found by inserting the first four orders in η of the form factors in given in Eq. (2.64), with $n = 0$ and $|m| \leq 2$, into the condition for the optimal Bell state fidelity (see Section 2.3.1 for more details). However, these errors are only optimal in the approximation of zero motional mode population $\bar{n} = 0$ and discounting the next orders of the Lamb-Dicke as well as the next orders in the Magnus expansion, which we discuss next.

Errors at $\hat{Z}_3$

In the following, we demonstrate the relevance of the higher orders of the Magnus expansion. We restrict the discussion of the error terms to a description of the operators appearing in the error terms and of which order in Ω and η the error terms are. The first-sideband term of $\hat{Z}_3$ (fourth row in Table 2.1) for a rectangular pulse takes the form

$$\hat{Z}_3^{(m=1)} = \hat{J}_y(\hat{a} + \hat{a}^\dagger)\mathcal{O}(\Omega^3\eta^5), \tag{2.71}$$

which gives $\mathcal{O}(\eta^2)$ at $\Omega = \Omega_{\mathrm{LD}}$. This term creates a phonon-assisted single-qubit flip. The second-sideband term for $\hat{Z}_3$ (fifth row in Table 2.1) is of order

$$\hat{Z}_3^{(m=2)} = \hat{J}_x\left(\mathbb{1} - \hat{J}_y^2\right)\left(\hat{a}^2 - (\hat{a}^\dagger)^2\right)\mathcal{O}(\Omega^3\eta^4), \tag{2.72}$$

which is $\mathcal{O}(\eta)$ at $\Omega = \Omega_{\mathrm{LD}}$. This term causes squeezing [KCM22] and population leakage into the motional mode. The energy level diagram in Fig. 2.1 depicts how the processes in $\hat{Z}_3$ cause population leakage in both the motional mode and qubit subspaces.

Errors and optimal drive amplitude at $\hat{\mathbf{Z}}_4$

The fourth order of the Magnus expansion is the sum of three entangling operations

$$\begin{aligned}\hat{Z}_4^{(m=1)} =& \hat{J}_{xy}\left(\hat{a}+\hat{a}^\dagger\right)\mathcal{O}(\Omega^4\eta^3)\\ &+\hat{J}_z^2\mathcal{O}(\Omega^4\eta^2)\\ &+\hat{J}_x^2\mathcal{O}(\Omega^4\eta^2),\end{aligned} \tag{2.73}$$

where

$$\hat{J}_{\alpha\beta}=\frac{1}{2}\left(\hat{\sigma}_\alpha\otimes\hat{\sigma}_\beta+\hat{\sigma}_\beta\otimes\hat{\sigma}_\alpha\right). \tag{2.74}$$

The full expressions are listed in rows 6–8 of Table 2.1. As sketched in Fig. 2.1, the first term in $\hat{Z}_4$, $\hat{J}_{xy}\left(\hat{a}+\hat{a}^\dagger\right)$, creates entanglement, but also causes population leakage in the motional mode. The second term, $\hat{J}_z^2$, adds a phase to the target state. The third term, $\hat{J}_y^2$, contributes to the entangling gate.

The leading terms of the first sideband order terms $\hat{Z}_2^{(m=1)}+\hat{Z}_2^{(m=2)}+\hat{Z}_4^{(m=1)}$ are $\mathcal{O}(\eta^4)$ and proportional to $\hat{J}_y^2$ or $\hat{J}_x^2$. Inserting the resulting prefactor

$$d_y^{(n)}=-\Omega^2T^2\frac{K\eta^2(\eta^2-1)}{\pi\left(K^2-L^2\right)}+\Omega^4T^4\frac{K\eta^2}{4\pi^3L^2\left(K^2-L^2\right)} \tag{2.75}$$

into the condition for the average fidelity, given in Eq. (2.61), and setting $\mathcal{F}=1$, yields a quadratic equation in Ω^2,

$$-\frac{\Omega^2T^2K\eta^2\left(4\pi^2L^2(\eta^2-1)+\Omega^2T^2\right)}{4\pi^3L^2(K^2-L^2)}=\frac{\pi}{2}, \tag{2.76}$$

whose solution is the corrected optimal drive amplitude

$$\Omega_4^2=\frac{\sqrt{2}\pi^2L\left(s-\sqrt{s^2-(K^2-L^2)}\right)}{\sqrt{K}T^2\eta}, \tag{2.77}$$

with $s=\sqrt{2K}L\eta(1-\eta^2)$. Note that this analytical value for the drive amplitude is calculated using various approximations and is therefore only valid for regimes where $s^2-(K^2-L^2)\geq 0$. For $\frac{K-L}{K}\ll 1$, this regime corresponds approximately to the condition $K^2\eta^2\geq K-L$. Hence, the expression for Ω_4 in Eq. (2.77) is only valid for sufficiently large η and K, otherwise the optimal value

for Ω_4 must be calculated numerically.

Since Ω_4 is $\mathcal{O}(\eta^{-\frac{1}{2}})$, in contrast to Ω_{LD} and Ω_2 which are $\mathcal{O}(\eta^{-1})$, the Lamb-Dicke orders of the terms of the Magnus expansion change when driving at Ω_4 instead of Ω_2 or Ω_{LD}, which is reflected in the last two columns of Table 2.1.

2.3.3. Numerical comparison

In the previous section, the analytical expressions for the leading error terms in the Magnus expansion were presented, summarized in Table 2.1. This section focuses on numerically analyzing the impact of these error terms on the average fidelity of the Mølmer-Sørensen gate. We compare the infidelities $1 - \mathcal{F}_{\mathrm{av}}$ calculated with different time evolution operators. The fidelity representing the effect of the nth order of the Magnus expansion is calculated with

$$\hat{U}_n := \exp\left\{-i \sum_{k=2}^{n} \hat{Z}_k\right\}. \tag{2.78}$$

The first order $\hat{Z}_1$ is always suppressed. The numerical expressions for the Magnus terms $\hat{Z}_n$ are calculated using the formulas shown in the previous sections. The operators are implemented in matrix form with the operators acting on the motional-mode subspace being truncated at $N_{\mathrm{dim}} = 8$. The resonance integrals are calculated recursively using computer tools as described in Section 2.2.

In the previous section, the analysis of the Magnus expansion orders was limited to the second to fourth order. To ensure the adequacy of this restriction, we calculate the infidelity including the fifth-order Magnus term as well, represented as $\hat{U}_5$. However, since the results show that the curves obtained with $\hat{U}_5$ nearly completely overlap with those calculated with $\hat{U}_4$ (see Fig. 2.2), indicating that $\hat{U}_n$ converges, the fifth order terms are not included in Figs. 2.3 to 2.8 in order to avoid visual clutter.

To evaluate the accuracy of a truncated propagator in representing the actual system evolution, we estimate the propagator for infinite Magnus orders $\hat{U}_\infty$. This estimation is accomplished through numerical calculation of the time evolution operator using the Trotter expansion [Tro59], which decomposes the propagator

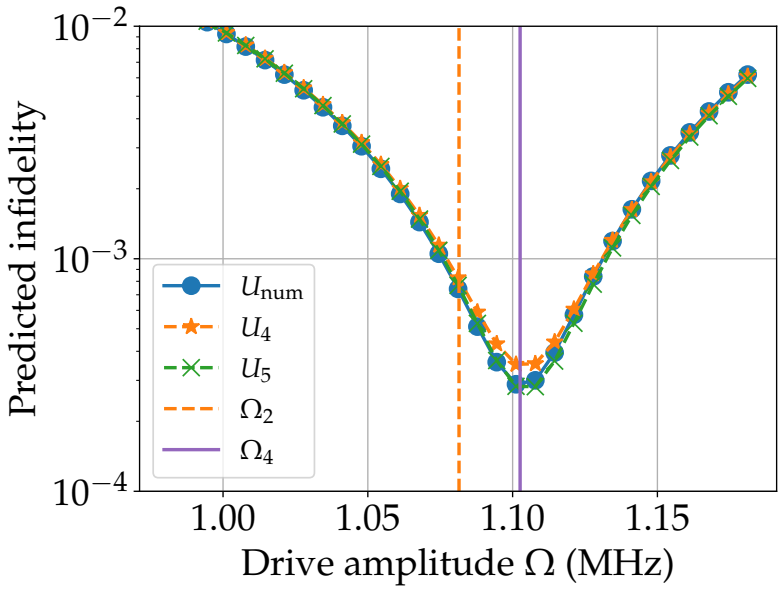

Figure 2.2.: Comparison of the infidelities calculated with $\hat{U}_4$ and $\hat{U}_5$ to the infidelities for $\hat{U}_{\text{num}}$. The curves for U_5 and U_{num} nearly completely overlap, while the minimal predicted infidelity (approximately 3.5×10^{-4}) for $\hat{U}_4$ differs slightly from the minimum of $\hat{U}_5$ and $_{\text{num}}$, which lies at approximately 3.5×10^{-4}.

into products of exponential operators, each corresponding to a small time step (see Section 2.1.1). We define the numerical propagator as

$$\hat{U}_{\text{num}} := \prod_{n=0}^{N_t} e^{-\frac{i}{\hbar} H(n\Delta t)\Delta t}. \tag{2.79}$$

To ensure that the time steps are sufficiently small, they are set to $\Delta t = \frac{1}{10 f_{\max}}$, where $f_{\max} = \max\{M + mK + L\}\frac{2\pi}{T}$ is the largest frequency appearing in the Hamiltonian, Eq. (2.32). As the Magnus expansion terms for the numerical calculations are truncated after the third sideband order, we set $m = 3$ in $f_{\max}$.

The Figs. 2.3, 2.4 and 2.7 were created using the following typical parameters [Meh+20; Zar+19; Won+17; Sch+18]: The Lamb-Dicke parameter is set to $\eta = 0.18$. The average trap population is chosen as $\bar{n} = 2 \times 10^{-2}$. For rectangular pulses, the dimensionless gate duration is $K = 28$, which corresponds to a gate duration of 28 µs for a trap frequency of $\nu/(2\pi) = 1$ MHz. The dimensionless laser detuning difference from the trap frequency, $K - L$, is set to 3, correspond-

ing to a detuning of 107 kHz, illustrating that the smallest detuning of $K - L$ may not always be optimal.

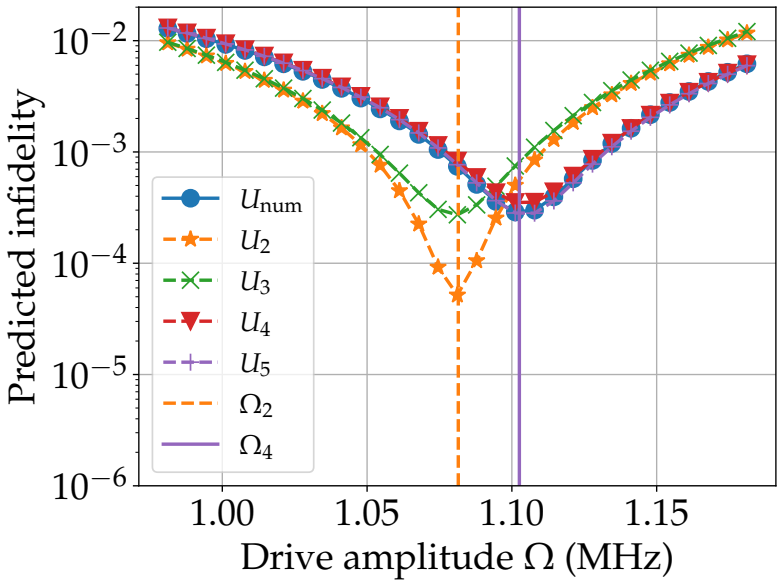

Figure 2.3.: Predicted average infidelity as a function of the drive amplitude Ω calculated with $\hat{U}_{\text{num}}$ and different Magnus expansion orders $\hat{U}_2$, $\hat{U}_3$, $\hat{U}_4$, and $\hat{U}_5$ in Eq. (2.78). The parameters are $\eta = 0.18$, $K - L = \frac{\nu-\delta}{2\pi}T$=3, $K = 28$, $\nu/(2\pi) = 1\,\text{MHz}$, and $\bar{n} = 2 \times 10^{-2}$. The theoretical prediction of Ω_2, see Eq. (2.70), is depicted with the dashed orange vertical line. The theoretical prediction of Ω_4, see Eq. (2.77), is shown with the solid red vertical line. The Magnus orders $\hat{Z}_k$ are calculated taking into account the first three sideband orders $|m_i| \leq 3$.

In Fig. 2.3, the predicted infidelities for the propagators $\hat{U}_n$ and $\hat{U}_{\text{num}}$ are displayed as a function of the drive amplitude Ω. The minima of the predicted infidelities calculated with $\hat{U}_2$ and $\hat{U}_3$, respectively, are approximately located at the drive amplitude Ω_2, whose value was calculated using Eq. (2.70). The curves for $\hat{U}_4$ and $\hat{U}_{\text{num}}$ are nearly indistinguishable at off-resonance and are closely aligned around their minimum, which is approximately at the expected optimal Rabi frequency Ω_4, calculated with Eq. (2.77).

The predicted infidelity of $\hat{U}_3$ at Ω_2 is approximately equal to the infidelities of $\hat{U}_4$ and $\hat{U}_{\text{num}}$ at Ω_4, indicating that $\hat{U}_3$ is limiting the achievable infidelity. For the sake of consistency, in Figs. 2.4, 2.5 and 2.7, we compare $\hat{U}_n$ to $\hat{U}_{\text{num}}$ with the drive amplitude set to $\Omega = \Omega_2$, but it is worth noting that the results are similar

for $\Omega = \Omega_4$.

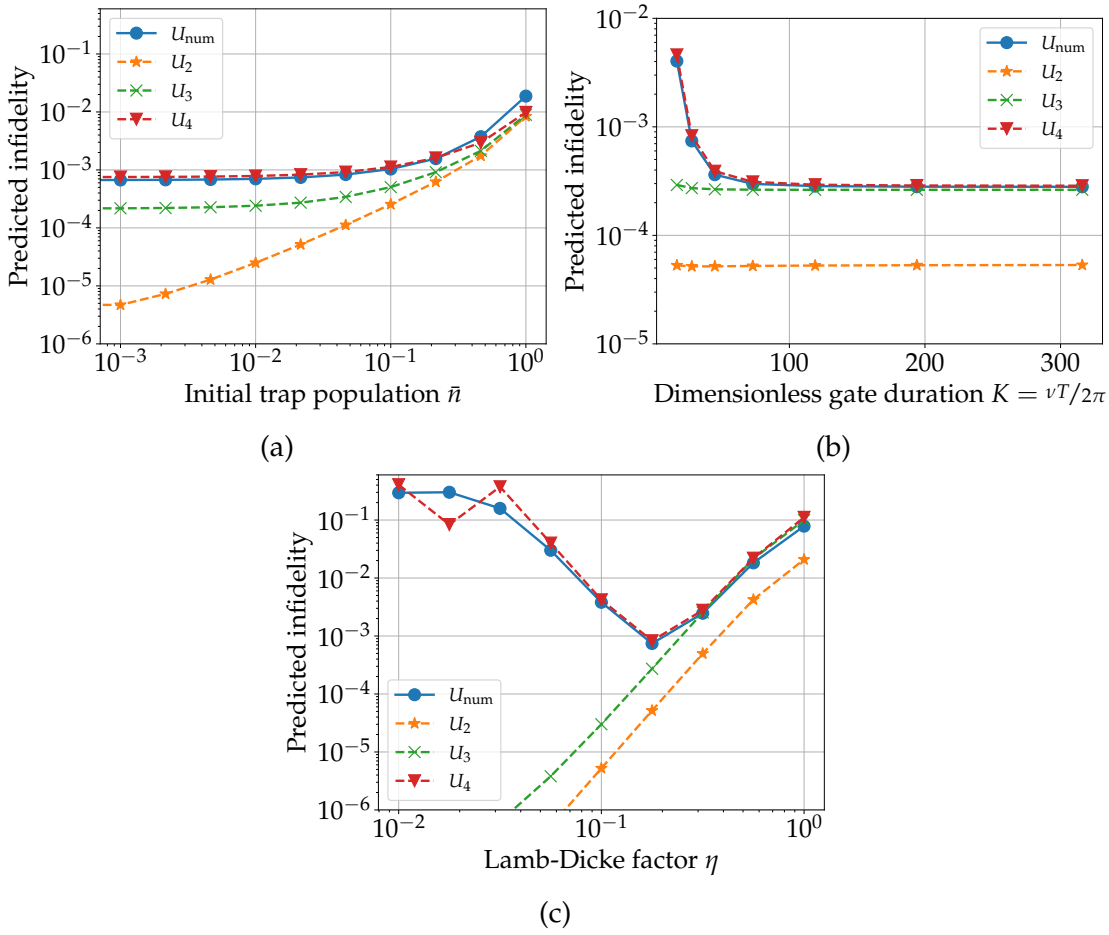

Figure 2.4.: Predicted average infidelity as a function of the population of the motional mode $\bar{n}$ (Fig. 2.4a), the dimensionless gate duration K (Fig. 2.4b), and the coupling strength η (Fig. 2.4c), respectively. The parameters are (if they are not varied): $\eta = 0.18$, $K - L = \frac{\nu-\delta}{2\pi}T = 3$, $K = 28$, $\nu/(2\pi) = 1\,\text{MHz}$, $\bar{n} = 2 \times 10^{-2}$, and $\Omega = \Omega_2$, defined in Eq. (2.70). The lines denoted with U_n and U_{num} are the predicted infidelities calculated with the propagators $\hat{U}_n$, given in Eq. (2.78) and $\hat{U}_{\text{num}}$, given in Eq. (2.79), respectively.

In the following, we provide a comparison between the infidelity calculated using different propagators as a function of various parameters, as shown in Fig. 2.4. As a general observation, Fig. 2.4 shows that there is a strong agreement between the curve calculated with $\hat{U}_4$ and with $\hat{U}_{\text{num}}$. The dependence of the infidelity on the average motional mode population is plotted in Fig. 2.4a. At low temperatures, the curves calculated with $\hat{U}_2$ and $\hat{U}_3$ predict lower infidelity than those

calculated with $\hat{U}_4$ and $\hat{U}_{\text{num}}$, highlighting their lack of predictive power. However, at higher temperature, all predicted infidelities increase monotonically and nearly converge. The infidelity is almost linear in the motional mode population $\bar{n}$, as expected from the terms that are linear in n, as shown in Table 2.1.

Figure 2.4b illustrates the predicted infidelity as a function of the dimensionless gate time $K = \frac{\nu T}{2\pi}$, indicating a quantum speed limit around $K = 100$, below which the predicted infidelity increases significantly as K decreases. For gate times longer than $K \approx 100$, the curves representing $\hat{U}_3$ and $\hat{U}_4$ converge, whereas for gate times shorter than $K \approx 100$, the predicted infidelities diverge, as expected when the coherent errors increase and the ratio of Ω to the other frequencies in the system is increased. In particular, the predicted infidelities calculated with $\hat{U}_4$ and $\hat{U}_{\text{num}}$ increase significantly as K decreases. Meanwhile, the infidelities calculated with the lower orders of the Magnus expansion $\hat{U}_2$ and $\hat{U}_3$ remain nearly horizontal, indicating an inability to capture the full dynamics at short times, but the curve calculated with $\hat{U}_2$ lies an order of magnitude below the infidelity calculated with U_3.

Figure 2.4c depicts the predicted infidelity as a function of the Lamb-Dicke parameter η. The curve calculated with $\hat{U}_2$ lies approximately an order of magnitude lower than the curve calculated with $\hat{U}_3$. The curves for $\hat{U}_4$ and $\hat{U}_{\text{num}}$ do approach the curve for $\hat{U}_3$ around $\eta = 0.3$, but this is in the higher error regime; on the other hand, they diverge significantly at smaller values of η, once again disagreeing strongly with the standard predictions. Notably, the curves calculated with $\hat{U}_2$ and $\hat{U}_3$ increase monotonically with η, while the curves calculated with $\hat{U}_4$ and $\hat{U}_{\text{num}}$ have a minimum around $\eta = 0.2$. This indicates that making the Lamb-Dicke parameter as small as possible does not improve the infidelity of the Mølmer-Sørensen gate. Instead, there is an optimal value for the Lamb-Dicke parameter for the Mølmer-Sørensen gate.

Fig. 2.5 shows that the value of the dimensionless detuning does not necessarily change the fidelity significantly. It depends strongly on the other parameters, whether an optimal value for $K - L$ is smaller or larger. Nonetheless, the value of $K - L$ is still restricted by the condition $\frac{K-L}{K} \ll 1$, which is crucial in the reasoning throughout this work (see Section 2.2.4), so we recommend strongly to choose a value for $K - L$ that remains in this limit.

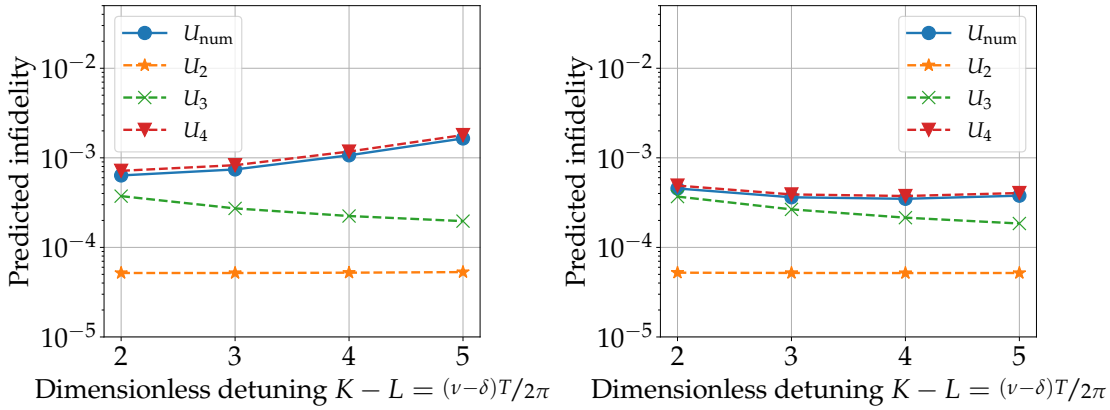

Figure 2.5.: Predicted average infidelity as a function of the dimensionless detuning $K - L$ at $K = 28$ (Fig. 2.5a) and $K = 45$ (Fig. 2.5b), respectively. The parameters are: $\eta = 0.18$, $\nu/(2\pi) = 1\,\text{MHz}$, $\bar{n} = 2 \times 10^{-2}$, and $\Omega = \Omega_2$, defined in Eq. (2.70). The lines denoted with U_n and U_{num} are the predicted infidelities calculated with the propagators $\hat{U}_n$, given in Eq. (2.78) and $\hat{U}_{\text{num}}$, given in Eq. (2.79), respectively.

2.3.4. Discussion

Terms of the Magnus expansion

In Fig. 2.1, the terms of Section 2.3 are visually represented. Through our analysis in the previous sections, it has become clear that the second order of the Magnus expansion $\hat{Z}_2$ is not the only term that significantly impacts the gate fidelity. In fact, terms up to and including the fourth order $\hat{Z}_4$ contribute significantly to the fidelity. Although higher orders in the Magnus expansion may in principle be relevant as well, in Section 2.3.3, we demonstrate that they are typically not necessary for commonly used parameters.

In a model that accounts only for the second order of the Magnus expansion, one might be tempted to choose a small value for the Lamb-Dicke parameter η to minimize errors related to the Lamb-Dicke expansion. However, as demonstrated in Table 2.1, reducing η decreases the error $\hat{Z}_2$ and $\hat{Z}_3$, but also increases the error term in $\hat{Z}_4$. This indicates the existence of a sweet spot for η, as shown in Fig. 2.4c. The fourth order term $\hat{Z}_4$ leads, due to the additional term proportional to $\hat{J}_y^2$, to a shift in the optimal drive amplitude without significantly impacting the fidelity compared to $\hat{Z}_3$. Meanwhile, the contribution of $\hat{Z}_3$, compared to $\hat{Z}_2$,

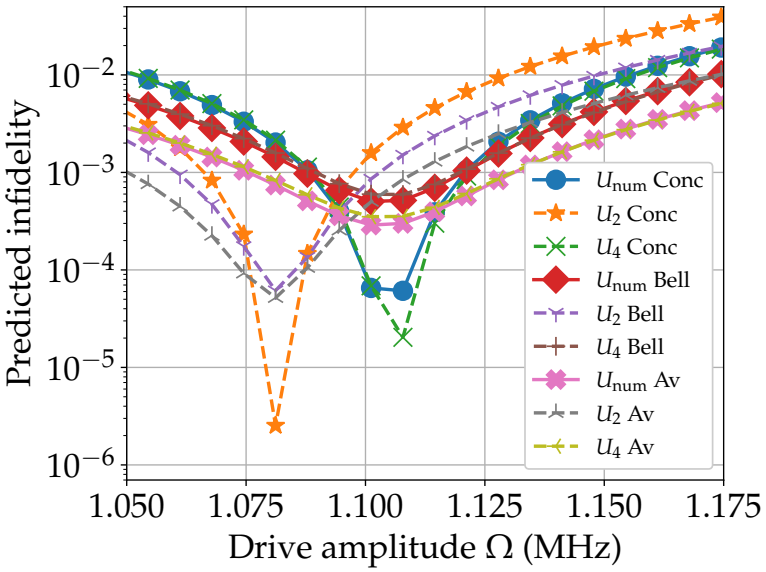

Figure 2.6.: Comparison of the results for concurrence and for Bell state and average infidelity as a function of the drive amplitude Ω, using the same parameters as in Fig. 2.4.

increases the infidelity, as illustrated in Table 2.1 and Fig. 2.3.

The temperature dependence of the error terms, as presented in Table 2.1, reveals that certain terms are proportional to $\bar{n}$, consistent with the trend observed in Fig. 2.4a.

According to [SM00], one can neglect $\hat{Z}_3$, because the error in $\hat{Z}_2$ is $\mathcal{O}(n\eta^2)$, while the error in $\hat{Z}_3$ is $\mathcal{O}(\eta^2)$. They argue that deviations of the Lamb-Dicke approximation are typically caused by large values of n, rather than η, making $\hat{Z}_3$ insignificant compared to $\hat{Z}_2$. Nevertheless, this perspective fails to consider that error terms related to higher sideband orders, as well as higher orders in the Magnus expansion, could have lower orders in the Lamb-Dicke expansion, as is in the case of the second sideband of $\hat{Z}_3$ and in $\hat{Z}_4$. Moreover, due to improved cooling methods [Meh+20] since then, it is increasingly crucial to have expressions that remain valid also at low temperatures.

Fidelity and optimal drive amplitude

As can be seen from Fig. 2.3, the drive amplitude leading to the lowest infidelity depends on the Magnus terms that are taken into account for the fidelity calculation. We show with the analytical expressions for the average and Bell fidelity, given in Eqs. (2.57) and (2.61), respectively, how the fourth order term $\hat{Z}_4$ contributes to the fidelity. The expression for the average fidelity only takes the form factor d_y into account. Thus, we used the average fidelity to derive the optimal drive amplitudes Ω_{LD} and Ω_4, since the dominant terms in the respective approximate effective Hamiltonians are proportional to $\hat{J}_y^2$. Because the approximate effective Hamiltonian, which is used to calculate Ω_2, contains terms proportional to $\hat{J}y^2$ as well as $\hat{J}_x^2$, the more general formula for the Bell fidelity comes in handy here.

Although the Bell state fidelity requires specification of initial and target state and the average fidelity requires a specific target gate, the results are nonetheless quite similar: For the parameters used in Fig. 2.4 at $\Omega = \Omega_2$, the Bell state infidelity is $1 - \mathcal{F}_{\mathrm{Bell}}(\hat{U}_{\mathrm{num}}) = 1.3 \times 10^{-3}$ and the average infidelity $1 - \mathcal{F}_{\mathrm{av}}(\hat{U}_{\mathrm{num}}) = 0.67 \times 10^{-3}$. At $\Omega = \Omega_4$ the infidelities are $1 - \mathcal{F}_{\mathrm{Bell}}(\hat{U}_{\mathrm{num}}) = 4.3 \times 10^{-4}$ and $1 - \mathcal{F}_{\mathrm{av}}(\hat{U}_{\mathrm{num}}) = 2.4 \times 10^{-4}$ for the Bell state infidelity and the average infidelity, respectively.

As plotted in Fig. 2.6, calculation of the concurrence, defined in Eq. (1.8), yields lower values for the infidelity, but shows minima at the same values for the drive amplitude Ω, indicating that the choice of fidelity does not affect the overall results of this work.

Beyond this discussion, the error budget terms presented in Table 2.1 provide the precise Hamiltonian description and do not hinge on a particular fidelity metric. As such, they are relevant to any particular cost function that is used.

2.4. Error terms for shaped drive pulses

So far, we have scrutinized the problem for a rectangular drive amplitude. However, the analysis in Section 2.2.5 shows that the results can be generalized to arbitrary finite-window, smooth pulse shapes. Amplitude modulation experiments

on the Mølmer-Sørensen gate have already been performed [Zar+19; Ste+14], but to the authors' knowledge, no theoretical investigation has been realized so far. A straightforward candidate for a smooth pulse is a Gaussian pulse, but since it is not finite in time, we fall back on a similar, but well-behaved, pulse shape of the form

$$\Omega(t) = \Omega \sin^2\left(\frac{\pi}{T}t\right). \tag{2.80}$$

The $\sin^2$ pulse shape also has a narrower bandwidth (i.e., smaller maximal value of M), when compared to a truncated Gaussian pulse. This is potentially preferable, since fewer unwanted transitions may be driven, and in general more compatible with keeping track of all the resonance conditions, which we discussed in Section 2.2.

2.4.1. Analytic expressions

In order to keep the following analytical expressions simple, some trivial resonances need to be avoided. As explained in Section 2.2.5, the resulting integer conditions are a bit more tedious for shaped pulses than for rectangular pulses. Hence, to avoid lengthy case distinctions in the general expressions for the Magnus terms, the following expressions are only valid under the conditions that we discuss in Section 2.2.5.

The second order of the Magnus expansion for a $\sin^2$ pulse shape is of the form

$$\begin{aligned}\hat{Z}_{2,\sin^2} = -\frac{K\Omega^2 T^2 \eta^2}{\pi}\Bigg(&\frac{p_y}{q_y}\left(1-(2n+1)\eta^2\right)\hat{J}_y^2 \\ &-\frac{p_x}{q_x}(2n+1)\,\eta^2\hat{J}_x^2\Bigg),\end{aligned} \tag{2.81}$$

where $p_{x,y}$ and $q_{x,y}$ are polynomials in K and L, defined as

$$p_y = 3\left(K^2-L^2\right)^2 - 4\left(5K^2+3L^2+8\right) \tag{2.82}$$

$$q_y = 8\left(K^2-L^2\right)\left((K-L)^2-4\right)\left((K+L)^2-4\right) \tag{2.83}$$

$$p_x = 0 \tag{2.84}$$

$$q_x = 0 \tag{2.85}$$

for the first sideband $\hat{Z}^{(m=1)}_{2,\sin^2}$.

The optimal drive amplitude (taking only the leading Lamb-Dicke order and the first sideband into account) is then

$$\Omega_{\mathrm{LD},\sin^2} = \frac{\pi}{\eta T\sqrt{2K}}\sqrt{\frac{q_y}{p_y}} \tag{2.86}$$

For the second sideband $\hat{Z}^{(m=2)}_{2,\sin^2}$, the coefficients p_x and q_x take non-zero values,

$$p_x = 8\left(6K^4 - 3K^2L^2 - 10K^2 + 4\right) + 3\left(L^4 - 4L^2\right) \tag{2.87}$$

$$q_x = 8\left(4K^2 - L^2\right)\left((2K-L)^2 - 4\right)\left((2K+L)^2 - 4\right), \tag{2.88}$$

while the values for p_y and q_y remain unchanged.

The third order of the Magnus expansion is of the form

$$\hat{Z}_{3,\sin^2} = \frac{K^2\Omega^3T^3\eta^5}{\pi^2}\frac{p_3}{q_3}\hat{J}_y\left(\hat{a} + \hat{a}^\dagger\right), \tag{2.89}$$

where p_3 and q_3 are again polynomials in K and L, defined as

$$p_3 = \left(K^2 + 3L^2 - 4\right)\left(3\left(K^2 - L^2\right)^2 - 4\left(5K^2 + 3L^2 - 8\right)\right) \tag{2.90}$$

$$q_3 = 2\left(K^2 - L^2\right)^2\left((K-L)^2 - 4\right)^2\left((K+L)^2 - 4\right)^2. \tag{2.91}$$

One can show that the resulting error terms at the optimal drive amplitude $\Omega_{\mathrm{LD},\sin^2}$ are smaller than the error terms for a rectangular pulse, which have the same form, but different prefactors. This is, because for most realistic choices of K and L, the prefactor $\frac{p_3}{q_3}$ is smaller when the system is driven with a $\sin^2$ pulse than the respective prefactor when driving with a rectangular pulse.

2.4.2. Numerical comparison

We now compare the average infidelity $1-\mathcal{F}$ using a rectangular pulse ($\Omega(t) = \Omega$) to the infidelity using a $\sin^2$ pulse ($\Omega(t) = \Omega\sin^2\left(\frac{\pi}{T}t\right)$). Explicitly, we com-

pare the propagators $\hat{U}_n$ with $n = 2, \cdots, 4$ to $\hat{U}_{\text{num}}$ for a system driven with a $\sin^2$ pulse, while also comparing to $\hat{U}_{\text{num}}$ for a system driven with constant drive amplitudes. The propagators $\hat{U}_n$, $\hat{U}_{\text{num}}$ are calculated using Eqs. (2.78) and (2.79), respectively.

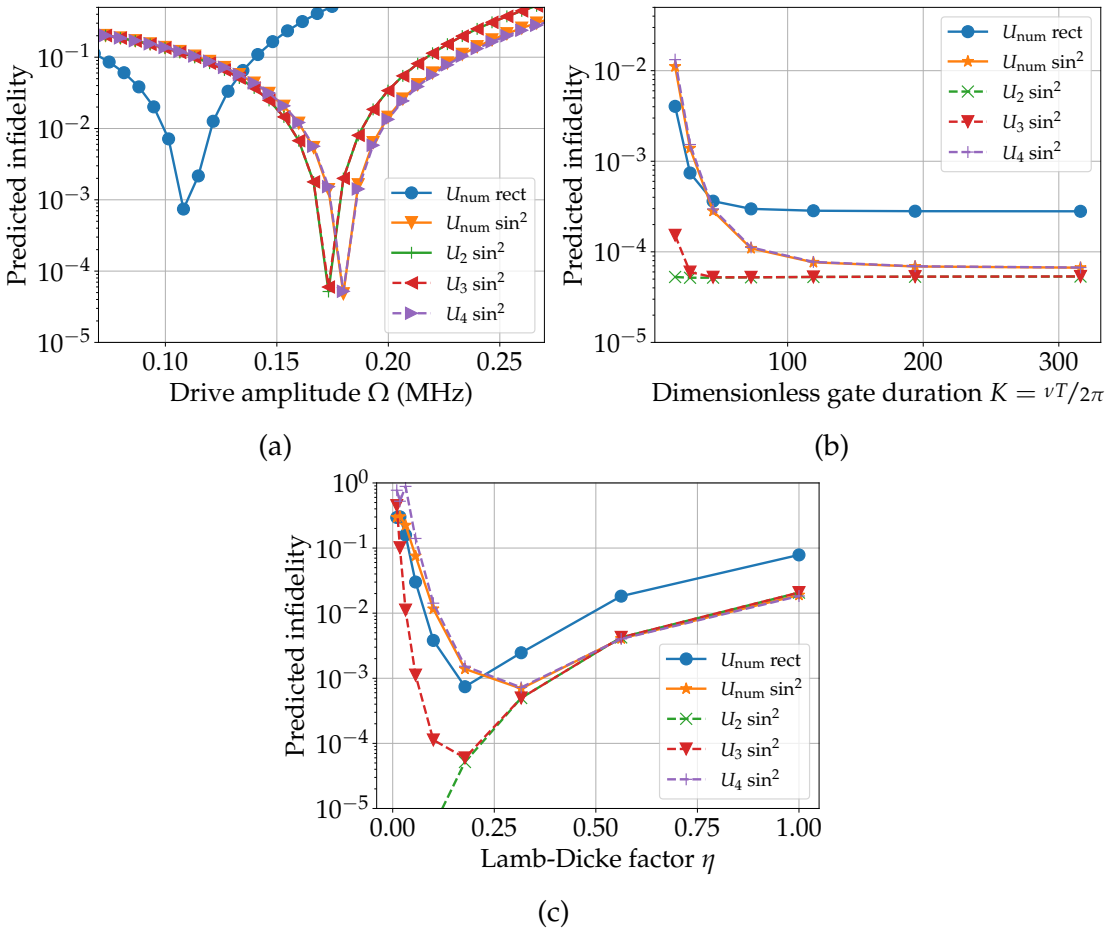

Figure 2.7.: Predicted average infidelity of the Mølmer-Sørensen gate driven using $\sin^2$ pulses as a function of drive amplitude Ω, dimensionless gate duration K and Lamb-Dicke factor η, respectively. For comparison the numerical predicted infidelity for a rectangular pulse is plotted as well. The parameters are (if they are not varied): $\eta = 0.18$, $K - L = \frac{\nu-\delta}{2\pi}T = 3$, $K = 28$, $\nu/(2\pi) = 0.1\,\text{MHz}$, $\bar{n} = 2 \times 10^{-2}$. The data for Figs. 2.7b and 2.7c is calculated using $\Omega = \Omega_{2,\text{rect}}$ for the rectangular pulse shape, calculated using Eq. (2.70), and using $\Omega = 0.173\,\text{MHz}$, corresponding to the minimum of the infidelity of $\hat{U}_2$ in Fig. 2.7a for the $\sin^2$ pulse shape.

Comparing the predicted infidelities calculated with $\hat{U}_{\text{num}}$ as a function of Ω for

a rectangular and a $\sin^2$ pulse, one can see in Fig. 2.7a that the optimal (highest fidelity reached) drive amplitude differs for different pulse shapes, but that the minimal predicted infidelity for a $\sin^2$ pulse is smaller than for a rectangular pulse. Because the optimal drive amplitudes differ for different pulse shapes, in Figs. 2.7b and 2.7c the fidelities are plotted at their respective optimal drive amplitude Ω_2, determined numerically from Fig. 2.7a.

In Fig. 2.7b, the infidelity is shown as a function of the dimensionless gate duration K. In the low infidelity regime, the shaped pulses outperform the square pulses considerably, with both the full numerics and the fourth Magnus order closely agreeing. The graph also shows that inclusion for orders higher than three in the Magnus expansion described by $\hat{U}_4$ results in an increase of the predicted infidelity as the value of K decreases, but only below a certain threshold that is dependent on η. At dimensionless gate times longer than $K \approx 50$, the calculation using a $\sin^2$ pulse predicts a lower infidelity compared to a rectangular pulse, but at gate times shorter than $K \approx 50$, the rectangular pulse yields a lower infidelity. One can see that for the $\sin^2$ pulse, except for short gate times, there is a close agreement between the curve calculated with $\hat{U}_2$ and with $\hat{U}_3$, unlike for the rectangular pulse, as shown in Fig. 2.4b, which implies that pulse shaping can probably compensate for the off-diagonal errors in $\hat{Z}_3$.

For the Lamb-Dicke parameter η, we see once again that the contributions of the higher orders in the Magnus expansion lead correctly to the existence of an optimal value for η, while instead the terms $\hat{Z}_2$ and $\hat{Z}_3$ decrease with decreasing η. The data in Fig. 2.7c is not detailed enough to tell which pulse shape in general leads to a smaller minimal predicted infidelity. For Lamb-Dicke parameters larger than the minimal value, the $\sin^2$ pulse yields a much lower infidelity, but for small η, the rectangular pulse provides a slightly smaller infidelity. The behavior of the infidelity as a function of η is similar for both rectangular pulses and $\sin^2$ pulses.

2.4.3. Discussion

Figure 2.7 illustrates the potential for using shaped pulses to further reduce the error in the Mølmer-Sørensen gate. At a quantitative level, we see that while in

the previous plots parameter searches limited infidelities to the 10^{-3} range, there are promising parameter regimes with $\sin^2$ pulses that lead to errors below 10^{-4}. This can be explained mathematically, through the Magnus expansion, as arising out of generally smaller prefactors in front of the same error operators terms.

In Fig. 2.8, the minimal infidelity at gate duration T is shown. Each data point depicts the lowest infidelity in the data set, which was used in Figs. 2.3 and 2.4, at a given gate duration, optimized over ν, δ, and η. In Fig. 2.8a we see that with small Lamb-Dicke factor η one can reach low infidelities, but only for longer gate durations. Larger values of η allow for shorter gate durations, but at the cost of higher infidelity. As shown in Fig. 2.8b, shaped $\sin^2$ pulses enable to decrease the infidelity about one to two orders of magnitude, where the optimal Lamb-Dicke factor takes larger values compared to the optimal results for rectangular pulses.

At a qualitative level, the behavior of the infidelity for varying parameters for a $\sin^2$ pulse is similar to the behavior of the infidelity with a rectangular pulse. Moreover, for certain parameter regimes, the rectangular pulses actually outperform the $\sin^2$-strategy. This is consistent both with conventional wisdom on pulse shaping and the nuances of the Mølmer-Sørensen gate. Indeed, square pulses are known to allow spectral hole burning through their characteristic sinc spectrum, while smooth pulses offer the possibility of reducing bandwidth overall and thereby avoid entire ranges of off-resonant errors. In the case of the Mølmer-Sørensen gate, the spectral conditions on beat-note frequencies not only reduce errors at low Magnus orders, but in certain cases also eliminate certain other terms, and so for a fortuitous choice of parameters it may indeed offer the best strategy. Smooth shaping allows nonetheless generally a safer option, and indeed seem to perform optimally in the best case. Lastly, the latter can be combined more easily with other control theoretic methods to potentially reduce errors even further.

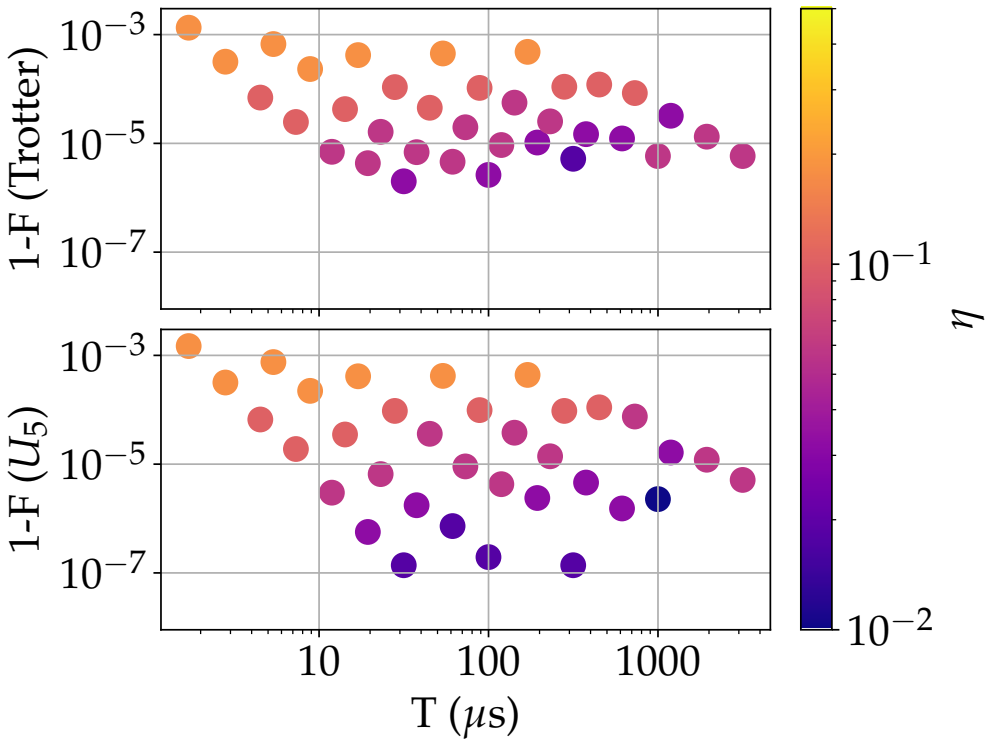

(a) Results for rectangular pulses.

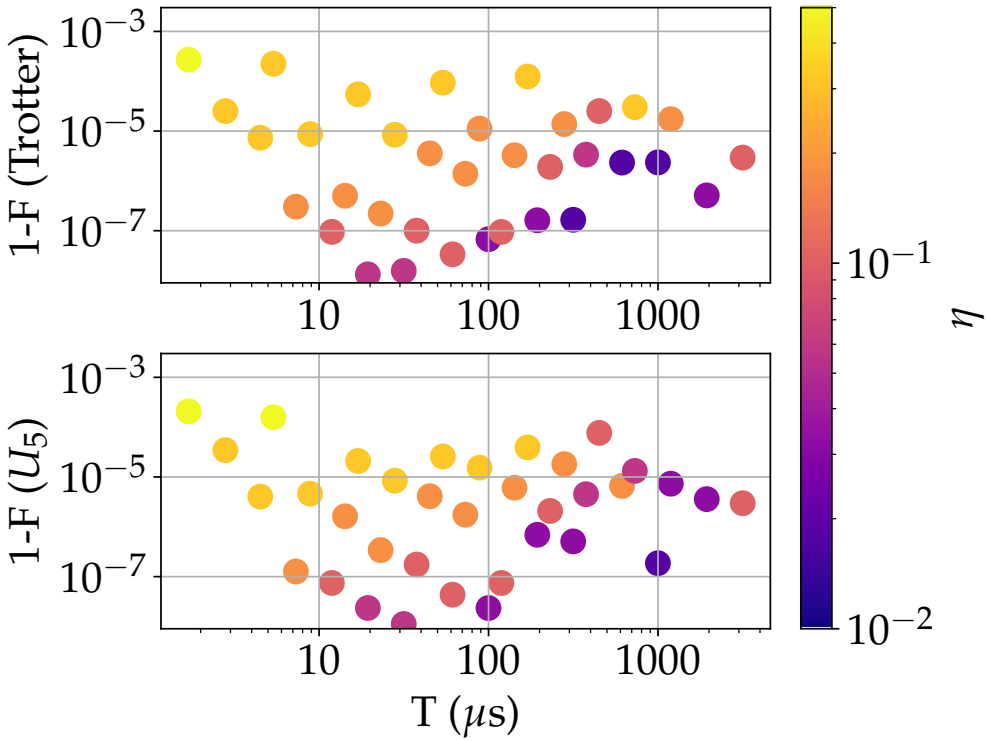

(b) Results for $\sin^2$ pulses.

Figure 2.8.: Minimal achieved infidelity, optimized over ν, $\bar{n}$, and η, as a function of the gate duration T. The value of η at minimal infidelity is color-coded. Top: Calculated using the Trotter propagator $\hat{U}_{\text{num}}$. Bottom: Calculated using the Magnus propagator $\hat{U}_5$.

Chapter 3.

Conclusion

Error correction in quantum computing and NISQ devices requires the implementation of two-qubit gates, such as the Mølmer-Sørensen gate, with sufficiently small infidelity. While some gate errors can be reduced with optimized experimental conditions, as cleaning the surface of an ion trap, others can be controlled via clever choice of parameters. A precise theoretical understanding of the error budget is thus of great importance.

In this work, we provided a detailed description of the inherent limitations of the Mølmer-Sørensen gate. We explained in detail the dependence of the different errors on various system parameters. In particular, our analysis revealed that the achievable infidelity increases as the gate duration decreases if the gate duration drops below a certain threshold value. However, we also demonstrated that this quantum speed limit can be mitigated with time-dependent drive-amplitude envelopes, specifically by employing a pulse of the form $\Omega(t) = \Omega \sin^2(\frac{\pi}{T}t)$. Our detailed description allows for more precise predictions on the infidelity and hence significantly more educated choices for system parameters. Notably, we give predictive expressions for the optimal drive amplitude Ω (up to experimental calibration), and show qualitatively that the achievable infidelity for a given gate duration is nonlinear in η, hence an optimal value for η can be obtained—for instance, through numerical calibration. Our numerical and analytical results yield expressions for optimal parameter values while pointing out inherent limitations on the Mølmer-Sørensen gate.

A detailed error budget for the Mølmer-Sørensen gate provides a solid founda-

tion for the application of various optimal control techniques for gate fidelity optimization. When the Mølmer-Sørensen gate is pushed towards its limit—in terms of gate duration and fidelity—it becomes increasingly important to be aware of higher order terms that have not been taken into account in previous approaches. With the provided insight into the underlying error mechanisms, it becomes possible to selectively suppress these errors.

Furthermore, the analysis of the Mølmer-Sørensen gate done in this thesis can be as well repeated for multichromatic pulses or different pulse shapes, easily assessing the utility of those methods.

Altogether, as a well-established gate, the Mølmer-Sørensen gate continues to hold great potential and we hope that this work provides researchers with the tools necessary to unlock its full capabilities.

Bibliography

[AB96] Dorit Aharonov and Michael Ben-Or. "Fault Tolerant Quantum Computation with Constant Error". Nov. 15, 1996. DOI: 10.48550/arXiv.quant-ph/9611025. Pre-published.

[AB99] Dorit Aharonov and Michael Ben-Or. "Fault-Tolerant Quantum Computation With Constant Error Rate". June 30, 1999. DOI: 10.48550/arXiv.quant-ph/9906129. Pre-published.

[ACC18] Ana Arnal, Fernando Casas, and Cristina Chiralt. "A General Formula for the Magnus Expansion in Terms of Iterated Integrals of Right-Nested Commutators". In: *Journal of Physics Communications* 2.3 (Mar. 14, 2018), p. 035024. DOI: 10.1088/2399-6528/aab291.

[AL18] Tameem Albash and Daniel A. Lidar. "Adiabatic Quantum Computation". In: *Reviews of Modern Physics* 90.1 (Jan. 29, 2018), p. 015002. DOI: 10.1103/RevModPhys.90.015002.

[Arr+18] I. Arrazola et al. "Pulsed Dynamical Decoupling for Fast and Robust Two-Qubit Gates on Trapped Ions". In: *Physical Review A* 97.5 (May 9, 2018), p. 052312. DOI: 10.1103/PhysRevA.97.052312.

[Aru+19] Frank Arute et al. "Quantum Supremacy Using a Programmable Superconducting Processor". In: *Nature* 574.7779 (Oct. 2019), pp. 505–510. DOI: 10.1038/s41586-019-1666-5.

[AS72] Milton Abramowitz and Irene A. Stegun. *Handbook of Mathematical Functions: With Formulas, Graphs and Mathematical Tables [Conference under the Auspices of the National Science Foundation and the Massachussetts Institute of Technology]*. 10th ed. Dover Books on Advanced Mathematics. New York, 1972. ISBN: 978-0-486-61272-0.

[AV76] C. Audoin and J. Vanier. "Atomic Frequency Standards and Clocks". In: *Journal of Physics E: Scientific Instruments* 9.9 (Sept. 1976), p. 697. DOI: 10.1088/0022-3735/9/9/001.

[Bal+16] C. J. Ballance et al. "High-Fidelity Quantum Logic Gates Using Trapped-Ion Hyperfine Qubits". In: *Physical Review Letters* 117.6 (Aug. 4, 2016), p. 060504. DOI: 10.1103/PhysRevLett.117.060504.

[Bar+19] R. Barends et al. "Diabatic Gates for Frequency-Tunable Superconducting Qubits". In: *Physical Review Letters* 123.21 (Nov. 19, 2019), p. 210501. DOI: 10.1103/PhysRevLett.123.210501.

[BBM92] Charles H. Bennett, Gilles Brassard, and N. David Mermin. "Quantum Cryptography without Bell's Theorem". In: *Physical Review Letters* 68.5 (Feb. 3, 1992), pp. 557–559. DOI: 10.1103/PhysRevLett.68.557.

[BCD02] Robin Blume-Kohout, Carlton M Caves, and Ivan H Deutsch. "Climbing Mount Scalable: Physical Resource Requirements for a Scalable Quantum Computer". In: (2002).

[Ben+08a] J. Benhelm et al. "Experimental quantum-information processing with $^{43}Ca^{+}$ ions". In: *Physical Review A* 77.6 (June 4, 2008), p. 062306. DOI: 10.1103/PhysRevA.77.062306.

[Ben+08b] Jan Benhelm et al. "Towards Fault-Tolerant Quantum Computing with Trapped Ions". In: *Nature Physics* 4.6 (2008), p. 463. DOI: 10.1038/nphys961.

[Ben+93] Charles H. Bennett et al. "Teleporting an Unknown Quantum State via Dual Classical and Einstein-Podolsky-Rosen Channels". In: *Physical Review Letters* 70.13 (Mar. 29, 1993), pp. 1895–1899. DOI: 10.1103/PhysRevLett.70.1895.

[Ber+12] A. Bermudez et al. "Robust Trapped-Ion Quantum Logic Gates by Continuous Dynamical Decoupling". In: *Physical Review A* 85.4 (Apr. 4, 2012), 040302(R). DOI: 10.1103/PhysRevA.85.040302.

[Ber+17] A. Bermudez et al. "Assessing the Progress of Trapped-Ion Processors Towards Fault-Tolerant Quantum Computation". In: *Physical Review X* 7.4 (Dec. 13, 2017), p. 041061. DOI: 10.1103/PhysRevX.7.041061.

[BGB10] Maxime Boissonneault, J. M. Gambetta, and Alexandre Blais. "Improved Superconducting Qubit Readout by Qubit-Induced Nonlinearities". In: *Physical Review Letters* 105.10 (Sept. 2, 2010), p. 100504. DOI: 10.1103/PhysRevLett.105.100504.

[Bih+04] Eli Biham et al. "Quantum Computing without Entanglement". In: *Theoretical Computer Science* 320.1 (June 12, 2004), pp. 15–33. DOI: 10.1016/j.tcs.2004.03.041.

[BKM16] Kenneth R. Brown, Jungsang Kim, and Christopher Monroe. "Co-Designing a Scalable Quantum Computer with Trapped Atomic Ions". In: *npj Quantum Information* 2.1 (Nov. 8, 2016), pp. 1–10. DOI: 10.1038/npjqi.2016.34.

[Bla+09] S. Blanes et al. "The Magnus Expansion and Some of Its Applications". In: *Physics Reports* 470.5 (Jan. 1, 2009), pp. 151–238. DOI: 10.1016/j.physrep.2008.11.001.

[Bla+98] S Blanes et al. "Magnus and Fer Expansions for Matrix Differential Equations: The Convergence Problem". In: *Journal of Physics A: Mathematical and General* 31.1 (Jan. 9, 1998), pp. 259–268. DOI: 10.1088/0305-4470/31/1/023.

[Bog+24] Michael Bogobowicz et al. *Steady Progress in Approaching Quantum Advantage | McKinsey*. Apr. 24, 2024. URL: https://www.mckinsey.com/capabilities/mckinsey-digital/our-insights/steady-progress-in-approaching-the-quantum-advantage (visited on 07/09/2024).

[Bra+24] Sergey Bravyi et al. "High-Threshold and Low-Overhead Fault-Tolerant Quantum Memory". In: *Nature* 627.8005 (Mar. 2024), pp. 778–782. DOI: 10.1038/s41586-024-07107-7.

[BW92] Charles H. Bennett and Stephen J. Wiesner. "Communication via One- and Two-Particle Operators on Einstein-Podolsky-Rosen States". In: *Physical Review Letters* 69.20 (Nov. 16, 1992), pp. 2881–2884. DOI: 10.1103/PhysRevLett.69.2881.

[CDG98] Claude Cohen-Tannoudji, Jacques Dupont-Roc, and Gilbert Grynberg. *Atom—Photon Interactions: Basic Process and Appilcations*. 1st ed. Apr. 27, 1998. ISBN: 978-3-527-41446-8. DOI: 10.1002/9783527617197.

[Cla+21] Craig R. Clark et al. "High-Fidelity Bell-State Preparation with $^{40}Ca^{+}$ Optical Qubits". In: *Physical Review Letters* 127.13 (Sept. 24, 2021), p. 130505. DOI: 10.1103/PhysRevLett.127.130505.

[Coh+15] I. Cohen et al. "Multi-Qubit Gate with Trapped Ions for Microwave and Laser-Based Implementation". In: *New Journal of Physics* 17.4 (Apr. 2015), p. 043008. DOI: 10.1088/1367-2630/17/4/043008.

[Con17] Emily Conover. *Quantum Computers Are about to Get Real*. June 29, 2017. URL: https://web.archive.org/web/20240604191538/https://www.sciencenews.org/article/quantum-computers-are-about-get-real (visited on 07/09/2024).

[CTV17] Earl T Campbell, Barbara M Terhal, and Christophe Vuillot. "Roads towards Fault-Tolerant Universal Quantum Computation". In: *Nature* 549.7671 (2017), pp. 172–179. DOI: 10.1038/nature23460.

[CWP17] J. Casanova, Z.-Y. Wang, and M. B. Plenio. "Arbitrary Nuclear-Spin Gates in Diamond Mediated by a Nitrogen-Vacancy-Center Electron Spin". In: *Physical Review A* 96.3 (Sept. 11, 2017), p. 032314. DOI: 10.1103/PhysRevA.96.032314.

[CZ95] J. I. Cirac and P. Zoller. "Quantum Computations with Cold Trapped Ions". In: *Phys. Rev. Lett.* 74.20 (May 1995), pp. 4091–4094. DOI: 10.1103/PhysRevLett.74.4091.

[DBE97] David Elieser Deutsch, Adriano Barenco, and Artur Ekert. "Universality in Quantum Computation". In: *Proceedings of the Royal Society of London. Series A: Mathematical and Physical Sciences* 449.1937 (Jan. 1997), pp. 669–677. DOI: 10.1098/rspa.1995.0065.

[Deh56] H. G. Dehmelt. "Paramagnetic Resonance Reorientation of Atoms and Ions Aligned by Electron Impact". In: *Physical Review* 103.4 (Aug. 15, 1956), pp. 1125–1126. DOI: 10.1103/PhysRev.103.1125.

[DiV00] David P. DiVincenzo. "The Physical Implementation of Quantum Computation". In: *Fortschritte der Physik* 48.9–11 (2000), pp. 771–783. DOI: 10.1002/1521-3978(200009)48:9/11<771::AID-PROP771>3.0.CO;2-E.

[Dod+02] Jennifer L. Dodd et al. "Universal Quantum Computation and Simulation Using Any Entangling Hamiltonian and Local Unitaries". In: *Physical Review A* 65.4 (Apr. 4, 2002), p. 040301. DOI: 10.1103/PhysRevA.65.040301.

[EJM98] Artur Ekert, Richard Jozsa, and P. Marcer. "Quantum Algorithms: Entanglement-Enhanced Information Processing [and Discussion]". In: *Philosophical Transactions: Mathematical, Physical and Engineering Sciences* 356.1743 (1998), pp. 1769–1782. DOI: 10.1098/rsta.1998.0248.

[Eke91] Artur K. Ekert. "Quantum Cryptography Based on Bell's Theorem". In: *Physical Review Letters* 67.6 (Aug. 5, 1991), pp. 661–663. DOI: 10.1103/PhysRevLett.67.661.

[Esc+03] Jürgen Eschner et al. "Laser Cooling of Trapped Ions". In: *JOSA B* 20.5 (May 1, 2003), pp. 1003–1015. DOI: 10.1364/JOSAB.20.001003.

[Fei+12] Jianjia Fei et al. "Mediated Gates between Spin Qubits". In: *Physical Review A* 86.6 (Dec. 26, 2012), p. 062328. DOI: 10.1103/PhysRevA.86.062328.

[Foo+05] Christopher J Foot et al. *Atomic Physics*. Vol. 7. 2005.

[Fow+12] Austin G. Fowler et al. "Surface Codes: Towards Practical Large-Scale Quantum Computation". In: *Physical Review A* 86.3 (Sept. 18, 2012), p. 032324. DOI: 10.1103/PhysRevA.86.032324.

[Gae+16] J. P. Gaebler et al. "High-Fidelity Universal Gate Set for $^{9}Be^{+}$ Ion Qubits". In: *Physical Review Letters* 117.6 (Aug. 4, 2016), p. 060505. DOI: 10.1103/PhysRevLett.117.060505.

[GAN14] I. M. Georgescu, S. Ashhab, and Franco Nori. "Quantum Simulation". In: *Reviews of Modern Physics* 86.1 (Mar. 10, 2014), pp. 153–185. DOI: 10.1103/RevModPhys.86.153.

[Ger+22] Lukas Gerster et al. "Experimental Bayesian Calibration of Trapped-Ion Entangling Operations". In: *PRX Quantum* 3.2 (June 8, 2022), p. 020350. DOI: 10.1103/PRXQuantum.3.020350.

[GFE09] D. Gross, S. T. Flammia, and J. Eisert. "Most Quantum States Are Too Entangled To Be Useful As Computational Resources". In: *Physical Review Letters* 102.19 (May 11, 2009), p. 190501. DOI: 10.1103/PhysRevLett.102.190501.

[Gid25] Craig Gidney. "How to Factor 2048 Bit RSA Integers with Less than a Million Noisy Qubits". May 21, 2025. DOI: 10.48550/arXiv.2505.15917. Pre-published.

[Goo+25] Google Quantum AI and Collaborators et al. "Quantum Error Correction below the Surface Code Threshold". In: *Nature* 638.8052 (Feb. 27, 2025), pp. 920–926. DOI: 10.1038/s41586-024-08449-y.

[Hal15] Brian C. Hall. *Lie Groups, Lie Algebras, and Representations: An Elementary Introduction*. Vol. 222. Graduate Texts in Mathematics. Cham, 2015. ISBN: 978-3-319-13466-6. DOI: 10.1007/978-3-319-13467-3.

[Har+16] T. P. Harty et al. "High-Fidelity Trapped-Ion Quantum Logic Using Near-Field Microwaves". In: *Physical Review Letters* 117.14 (Sept. 27, 2016), p. 140501. DOI: 10.1103/PhysRevLett.117.140501.

[Har+20] Charles R. Harris et al. "Array Programming with NumPy". In: *Nature* 585.7825 (Sept. 17, 2020), pp. 357–362. DOI: 10.1038/s41586-020-2649-2.

[Hei+19] D Heinrich et al. "Ultrafast coherent excitation of a $^{40}Ca^{+}$ ion". In: *New Journal of Physics* 21.7 (July 1, 2019), p. 073017. DOI: 10.1088/1367-2630/ab2a7e.

[HK21] Kentaro Heya and Naoki Kanazawa. "Cross-Cross Resonance Gate". In: *PRX Quantum* 2.4 (Nov. 16, 2021), p. 040336. DOI: 10.1103/PRXQuantum.2.040336.

[Hor+09] Ryszard Horodecki et al. “Quantum Entanglement”. In: *Reviews of Modern Physics* 81.2 (June 17, 2009), pp. 865–942. DOI: 10.1103/RevModPhys.81.865.

[HRB08] H. Häffner, C. F. Roos, and R. Blatt. “Quantum Computing with Trapped Ions”. In: *Physics Reports* 469.4 (Dec. 1, 2008), pp. 155–203. DOI: 10.1016/j.physrep.2008.09.003.

[Ita+91] Wayne M. Itano et al. “Laser Cooling of Trapped Ions”. In: *NIST*. Laser Manipulation of Atoms and Ions (Enrico Fermi Summer School Jan. 1, 1991), pp. 519–537. URL: https://www.nist.gov/publications/laser-cooling-trapped-ions (visited on 04/25/2025).

[Jai+24] Shreyans Jain et al. “Penning Micro-Trap for Quantum Computing”. In: *Nature* 627.8004 (Mar. 2024), pp. 510–514. DOI: 10.1038/s41586-024-07111-x.

[Jam98] Daniel F. V. James. “Theory of Heating of the Quantum Ground State of Trapped Ions”. In: *Physical Review Letters* 81.2 (July 13, 1998), pp. 317–320. DOI: 10.1103/PhysRevLett.81.317.

[Jer+24] M. Jerger et al. “Dispersive Qubit Readout with Intrinsic Resonator Reset”. June 10, 2024. DOI: 10.48550/arXiv.2406.04891. Prepublished.

[Jia+23] Zhubing Jia et al. “Angle-Robust Two-Qubit Gates in a Linear Ion Crystal”. In: *Physical Review A* 107.3 (Mar. 23, 2023), p. 032617. DOI: 10.1103/PhysRevA.107.032617.

[JL03] Richard Jozsa and Noah Linden. “On the Role of Entanglement in Quantum-Computational Speed-Up”. In: *Proceedings of the Royal Society of London. Series A: Mathematical, Physical and Engineering Sciences* (Aug. 8, 2003). DOI: 10.1098/rspa.2002.1097.

[Kan+21] Mingyu Kang et al. “Batch Optimization of Frequency-Modulated Pulses for Robust Two-Qubit Gates in Ion Chains”. In: *Physical Review Applied* 16.2 (Aug. 24, 2021), p. 024039. DOI: 10.1103/PhysRevApplied.16.024039.

[Kas50] Alfred Kastler. "Quelques suggestions concernant la production optique et la détection optique d'une inégalité de population des niveaux de quantifigation spatiale des atomes. Application à l'expérience de Stern et Gerlach et à la résonance magnétique". In: *Journal de Physique et le Radium* 11.6 (1950), p. 255. DOI: 10.1051/jphysrad:01950001106025500.

[Kau+17] H. Kaufmann et al. "Scalable Creation of Long-Lived Multipartite Entanglement". In: *Physical Review Letters* 119.15 (Oct. 13, 2017), p. 150503. DOI: 10.1103/PhysRevLett.119.150503.

[KCM22] Or Katz, Marko Cetina, and Christopher Monroe. "N-Body Interactions between Trapped Ion Qubits via Spin-Dependent Squeezing". In: *Physical Review Letters* 129.6 (Aug. 4, 2022), p. 063603. DOI: 10.1103/PhysRevLett.129.063603.

[Kre+05] A. Kreuter et al. "Experimental and theoretical study of the $3d\ ^2D$–level lifetimes of $^{40}Ca^+$". In: *Physical Review A* 71.3 (Mar. 11, 2005), p. 032504. DOI: 10.1103/PhysRevA.71.032504.

[LCM24] Boxi Li, Tommaso Calarco, and Felix Motzoi. "Experimental Error Suppression in Cross-Resonance Gates via Multi-Derivative Pulse Shaping". In: *npj Quantum Information* 10.1 (July 2, 2024), pp. 1–10. DOI: 10.1038/s41534-024-00863-4.

[Lei+03] D. Leibfried et al. "Quantum Dynamics of Single Trapped Ions". In: *Reviews of Modern Physics* 75.1 (Mar. 10, 2003), pp. 281–324. DOI: 10.1103/RevModPhys.75.281.

[Lev08] Malcolm H. Levitt. *Spin Dynamics: Basics of Nuclear Magnetic Resonance*. 2nd ed. Chichester, England, 2008. ISBN: 978-0-470-51118-3.

[LM20] Jake Lishman and Florian Mintert. "Trapped-Ion Entangling Gates Robust against Qubit Frequency Errors". In: *Physical Review Research* 2.3 (July 22, 2020), p. 033117. DOI: 10.1103/PhysRevResearch.2.033117.

[LP01] Noah Linden and Sandu Popescu. "Good Dynamics versus Bad Kinematics: Is Entanglement Needed for Quantum Computation?" In: *Physical Review Letters* 87.4 (July 10, 2001), p. 047901. DOI: 10.1103/PhysRevLett.87.047901.

[Mad+22] Lars S. Madsen et al. "Quantum Computational Advantage with a Programmable Photonic Processor". In: *Nature* 606.7912 (June 2022), pp. 75–81. DOI: 10.1038/s41586-022-04725-x.

[Mag54] Wilhelm Magnus. "On the Exponential Solution of Differential Equations for a Linear Operator". In: *Communications on Pure and Applied Mathematics* 7.4 (Nov. 1954), pp. 649–673. DOI: 10.1002/cpa.3160070404.

[Mar+22] Fernando Martínez-García et al. "Analytical and Experimental Study of Center-Line Miscalibrations in Mølmer-Sørensen Gates". In: *Physical Review A* 105.3 (Mar. 23, 2022), p. 032437. DOI: 10.1103/PhysRevA.105.032437.

[McG+24] Catherine C. McGeoch et al. "A Comment on Comparing Optimization on D-Wave and IBM Quantum Processors". June 27, 2024. DOI: 10.48550/arXiv.2406.19351. Pre-published.

[MD68] F. G. Major and H. G. Dehmelt. "Exchange-Collision Technique for the Rf Spectroscopy of Stored Ions". In: *Physical Review* 170.1 (June 5, 1968), pp. 91–107. DOI: 10.1103/PhysRev.170.91.

[Meh+19] Karan K. Mehta et al. "Towards Fast and Scalable Trapped-Ion Quantum Logic with Integrated Photonics". In: *Advances in Photonics of Quantum Computing, Memory, and Communication XII*. SPIE OPTO. Vol. 10933. San Francisco, California, United States, Mar. 4, 2019, pp. 24–34. DOI: 10.1117/12.2507647.

[Meh+20] Karan K. Mehta et al. "Integrated Optical Multi-Ion Quantum Logic". In: *Nature* 586.7830 (Oct. 22, 2020), pp. 533–537. DOI: 10.1038/s41586-020-2823-6.

[Meu+17] Aaron Meurer et al. "SymPy: Symbolic Computing in Python". In: *PeerJ Computer Science* 3 (Jan. 2, 2017), e103. DOI: 10.7717/peerj-cs.103.

[Mos+23] S. A. Moses et al. "A Race-Track Trapped-Ion Quantum Processor". In: *Physical Review X* 13.4 (Dec. 18, 2023), p. 041052. DOI: 10.1103/PhysRevX.13.041052.

[Mye+08] A. H. Myerson et al. "High-Fidelity Readout of Trapped-Ion Qubits". In: *Physical Review Letters* 100.20 (May 23, 2008), p. 200502. DOI: 10.1103/PhysRevLett.100.200502.

[NC10] Michael A. Nielsen and Isaac L. Chuang. *Quantum Computation and Quantum Information*. 10th anniversary ed. Cambridge ; New York, 2010. 676 pp. ISBN: 978-1-107-00217-3.

[Neg+21] V. Negîrneac et al. "High-Fidelity Controlled-Z Gate with Maximal Intermediate Leakage Operating at the Speed Limit in a Superconducting Quantum Processor". In: *Physical Review Letters* 126.22 (June 4, 2021), p. 220502. DOI: 10.1103/PhysRevLett.126.220502.

[Neu+78] W. Neuhauser et al. "Optical-Sideband Cooling of Visible Atom Cloud Confined in Parabolic Well". In: *Physical Review Letters* 41.4 (July 24, 1978), pp. 233–236. DOI: 10.1103/PhysRevLett.41.233.

[NSD86] Warren Nagourney, Jon Sandberg, and Hans Dehmelt. "Shelved Optical Electron Amplifier: Observation of Quantum Jumps". In: *Physical Review Letters* 56.26 (June 30, 1986), pp. 2797–2799. DOI: 10.1103/PhysRevLett.56.2797.

[Olm+07] S. Olmschenk et al. "Manipulation and detection of a trapped Yb^+ hyperfine qubit". In: *Physical Review A* 76.5 (Nov. 19, 2007), p. 052314. DOI: 10.1103/PhysRevA.76.052314.

[Osp+11] C. Ospelkaus et al. "Microwave Quantum Logic Gates for Trapped Ions". In: *Nature* 476.7359 (Aug. 2011), pp. 181–184. DOI: 10.1038/nature10290.

[Pae+24] A. Paetznick et al. "Demonstration of Logical Qubits and Repeated Error Correction with Better-than-Physical Error Rates". Nov. 17, 2024. DOI: 10.48550/arXiv.2404.02280. Pre-published.

[Pai+16] Hanhee Paik et al. "Experimental Demonstration of a Resonator-Induced Phase Gate in a Multiqubit Circuit-QED System". In: *Physical Review Letters* 117.25 (Dec. 13, 2016), p. 250502. DOI: 10.1103/PhysRevLett.117.250502.

[Ped+19] Edwin Pednault et al. "Leveraging Secondary Storage to Simulate Deep 54-Qubit Sycamore Circuits". Oct. 22, 2019. DOI: 10.48550/arXiv.1910.09534. Pre-published.

[PKL22] Hélène Perrin, Robin Kaiser, and Michèle Leduc. *Ultra-Cold Atoms, Ions, Molecules and Quantum Technologies*. Les Ulis, FRANCE, 2022. ISBN: 978-2-7598-2746-6. URL: http://ebookcentral.proquest.com/lib/fz/detail.action?docID=30800070 (visited on 01/15/2025).

[Pre18] John Preskill. "Quantum Computing in the NISQ Era and Beyond". In: *Quantum* 2 (Aug. 6, 2018), p. 79. DOI: 10.22331/q-2018-08-06-79.

[PS53] Wolfgang Paul and Helmut Steinwedel. "Notizen: Ein Neues Massenspektrometer Ohne Magnetfeld". In: *Zeitschrift für Naturforschung A* 8.7 (July 1, 1953), pp. 448–450. DOI: 10.1515/zna-1953-0710.

[PV06] Martin B. Plenio and S. Virmani. "An Introduction to Entanglement Measures". June 10, 2006. DOI: 10.48550/arXiv.quant-ph/0504163. Pre-published.

[RB01] Robert Raussendorf and Hans J. Briegel. "A One-Way Quantum Computer". In: *Physical Review Letters* 86.22 (May 28, 2001), pp. 5188–5191. DOI: 10.1103/PhysRevLett.86.5188.

[Rea+18] Matthew Reagor et al. "Demonstration of Universal Parametric Entangling Gates on a Multi-Qubit Lattice". In: *Science Advances* 4.2 (Feb. 2, 2018), eaao3603. DOI: 10.1126/sciadv.aao3603.

[Ree+10] M. D. Reed et al. "High-Fidelity Readout in Circuit Quantum Electrodynamics Using the Jaynes-Cummings Nonlinearity". In: *Physical Review Letters* 105.17 (Oct. 19, 2010), p. 173601. DOI: 10.1103/PhysRevLett.105.173601.

[RGF03] Saar Rahav, Ido Gilary, and Shmuel Fishman. "Effective Hamiltonians for Periodically Driven Systems". In: *Physical Review A* 68.1 (July 28, 2003), p. 013820. DOI: 10.1103/PhysRevA.68.013820.

[RH07] Robert Raussendorf and Jim Harrington. "Fault-Tolerant Quantum Computation with High Threshold in Two Dimensions". In: *Physical Review Letters* 98.19 (May 11, 2007), p. 190504. DOI: 10.1103/PhysRevLett.98.190504.

[Sac+24] Natasha Sachdeva et al. "Quantum Optimization Using a 127-Qubit Gate-Model IBM Quantum Computer Can Outperform Quantum Annealers for Nontrivial Binary Optimization Problems". Oct. 28, 2024. DOI: 10.48550/arXiv.2406.01743. Pre-published.

[Sal85] W. R. Salzman. "An Alternative to the Magnus Expansion in Time-Dependent Perturbation Theory". In: *The Journal of Chemical Physics* 82.2 (Jan. 15, 1985), pp. 822–826. DOI: 10.1063/1.448508.

[San+23] S. Saner et al. "Breaking the Entangling Gate Speed Limit for Trapped-Ion Qubits Using a Phase-Stable Standing Wave". In: *Physical Review Letters* 131.22 (Dec. 1, 2023), p. 220601. DOI: 10.1103/PhysRevLett.131.220601.

[Sch+03a] F. Schmidt-Kaler et al. "How to Realize a Universal Quantum Gate with Trapped Ions". In: *Applied Physics B* 77.8 (Dec. 2003), pp. 789–796. DOI: 10.1007/s00340-003-1346-9.

[Sch+03b] Ferdinand Schmidt-Kaler et al. "Realization of the Cirac–Zoller Controlled-NOT Quantum Gate". In: *Nature* 422.6930 (Mar. 2003), pp. 408–411. DOI: 10.1038/nature01494.

[Sch+13] Philipp Schindler et al. "A Quantum Information Processor with Trapped Ions". In: *New Journal of Physics* 15.12 (Dec. 6, 2013), p. 123012. DOI: 10.1088/1367-2630/15/12/123012.

[Sch+18] V. M. Schäfer et al. "Fast Quantum Logic Gates with Trapped-Ion Qubits". In: *Nature* 555.7694 (Mar. 2018), pp. 75–78. DOI: 10.1038/nature25737.

[Sin14] Alastair Sinclair. "An Introduction to Trapped Ions, Scalability and Quantum Metrology". In: *Quantum Information and Coherence*. Ed. by Erika Andersson and Patrik Öhberg. Cham, 2014, pp. 211–245. ISBN: 978-3-319-04063-9. DOI: 10.1007/978-3-319-04063-9_9.

[SM00] Anders Sørensen and Klaus Mølmer. "Entanglement and Quantum Computation with Ions in Thermal Motion". In: *Physical Review A* 62.2 (July 18, 2000), p. 022311. DOI: 10.1103/PhysRevA.62.022311.

[SM99] Anders Sørensen and Klaus Mølmer. "Quantum Computation with Ions in Thermal Motion". In: *Physical Review Letters* 82.9 (Mar. 1, 1999), pp. 1971–1974. DOI: 10.1103/PhysRevLett.82.1971.

[SQ17] James D. Siverns and Qudsia Quraishi. "Ion Trap Architectures and New Directions". In: *Quantum Information Processing* 16.12 (Nov. 13, 2017), p. 314. DOI: 10.1007/s11128-017-1760-2.

[ST94] J. J. Sakurai and San Fu Tuan. *Modern Quantum Mechanics*. Rev. ed. Reading, Mass, 1994. 500 pp. ISBN: 978-0-201-53929-5.

[Ste+14] A. M. Steane et al. "Pulsed Force Sequences for Fast Phase-Insensitive Quantum Gates in Trapped Ions". In: *New Journal of Physics* 16.5 (May 2014), p. 053049. DOI: 10.1088/1367-2630/16/5/053049.

[Sti+06] D. Stick et al. "Ion Trap in a Semiconductor Chip". In: *Nature Physics* 2.1 (Jan. 2006), pp. 36–39. DOI: 10.1038/nphys171.

[Tin+21] Holly N. Tinkey et al. "Quantum Process Tomography of a Mølmer-Sørensen Gate via a Global Beam". In: *Quantum Science and Technology* 6.3 (June 2021), p. 034013. DOI: 10.1088/2058-9565/ac0543.

[Tro59] H. F. Trotter. "On the Product of Semi-Groups of Operators". In: *Proceedings of the American Mathematical Society* 10.4 (1959), pp. 545–551. DOI: 10.1090/S0002-9939-1959-0108732-6.

[Val+22] C. H. Valahu et al. "Quantum Control Methods for Robust Entanglement of Trapped Ions". In: *Journal of Physics B: Atomic, Molecular and Optical Physics* 55.20 (Sept. 2022), p. 204003. DOI: 10.1088/1361-6455/ac8eff.

[War84] Warren S. Warren. "Effects of Arbitrary Laser or NMR Pulse Shapes on Population Inversion and Coherence". In: *The Journal of Chemical Physics* 81.12 (Dec. 20, 1984), pp. 5437–5448. DOI: 10.1063/1.447644.

[Web+24] M. A. Weber et al. “Robust and Fast Microwave-Driven Quantum Logic for Trapped-Ion Qubits”. In: *Physical Review A* 110.1 (July 8, 2024), p. L010601. DOI: 10.1103/PhysRevA.110.L010601.

[WI79] D. J. Wineland and Wayne M. Itano. “Laser Cooling of Atoms”. In: *Physical Review A* 20.4 (Oct. 1, 1979), pp. 1521–1540. DOI: 10.1103/PhysRevA.20.1521.

[Win+98] D.J. Wineland et al. “Experimental Issues in Coherent Quantum-State Manipulation of Trapped Atomic Ions”. In: *Journal of Research of the National Institute of Standards and Technology* 103.3 (May 1998), p. 259. DOI: 10.6028/jres.103.019.

[Won+17] J. D. Wong-Campos et al. “Demonstration of Two-Atom Entanglement with Ultrafast Optical Pulses”. In: *Physical Review Letters* 119.23 (Dec. 8, 2017), p. 230501. DOI: 10.1103/PhysRevLett.119.230501.

[Zar+19] G. Zarantonello et al. “Robust and Resource-Efficient Microwave Near-Field Entangling $^{9}Be^{+}$ Gate”. In: *Physical Review Letters* 123.26 (Dec. 26, 2019), p. 260503. DOI: 10.1103/PhysRevLett.123.260503.

Appendix

A. Calculate nested integrals of products between exponential and power functions

The analytical expressions presented in Table 2.1 for the nested resonance integral given in Eq. (2.35) were computed using the SymPy software package [Meu+17]. The analytical evaluation of nested integrals with quickly oscillating integrands using computer algebra systems is a non-trivial task, particularly when some exponents are equal to zero, suppressing conditionally some of the oscillations, and thus making careful case distinctions necessary. To compute an analytic expression of a general nested resonance integral with k integrands, we applied the following algorithm:

---

function $I_{N_k,\cdots,N_1}(t,\mathrm{b})$
  if k=1 **then**
    if $N_1 = 0$ **then**
      return t
    else
      return $\frac{1}{bN_1}\left(e^{bN_1 t} - 1\right)$
    end if
  else
    $I_{k-1} := I_{N_{k-1},\cdots,N_1}(t_k,\mathrm{b})$
    return PRODINT$(t,\, e^{bN_k t_k} I_{k-1})$
  end if
end function
function PRODINT$(t, f(\tau))$
  Decompose $f(\tau)$ into a sum of the form $\sum e^{g}\tau^{m}$
  Integrate from 0 to t using integration by parts
  return integration result
end function

This algorithm recursively evaluates the nested integral while taking care of the oscillating terms. At each iteration, the term is decomposed into a sum of exponential functions multiplied by a polynomial. Each of these terms can be integrated using integration by parts. By keeping track of the arguments of the exponential and the polynomial function, the function returns an expression containing only exponential and polynomial functions, whose exact form depends on the arguments of the nested integral. These calculations are employed using

a custom-written Python class that implements integration by parts for functions of this specific form. The resulting expression can then be simplified using SymPy, which takes care of the case distinctions, making the final expressions more concise.

B. Further numerical evidence

The predicted infidelity calculated with $\hat{U}_{\text{num}}$, $\hat{U}_4$, and $\hat{U}_2$ is presented in Fig. B.1 as a function of η and K. Under identical parameter conditions, the results for shaped pulses and rectangular pulses at $\Omega = \Omega_2$ show a close similarity. Notably, the results for U_4 and U_{num} are nearly identical, suggesting a high degree of accuracy of the analytical terms. As expected, the data indicates that longer gate durations result in smaller infidelities. Furthermore, the results suggest that a different optimal Lamb-Dicke parameter exists for each gate duration, a trend that is not apparent in the data and analytical expressions obtained using solely $\hat{U}_2$.

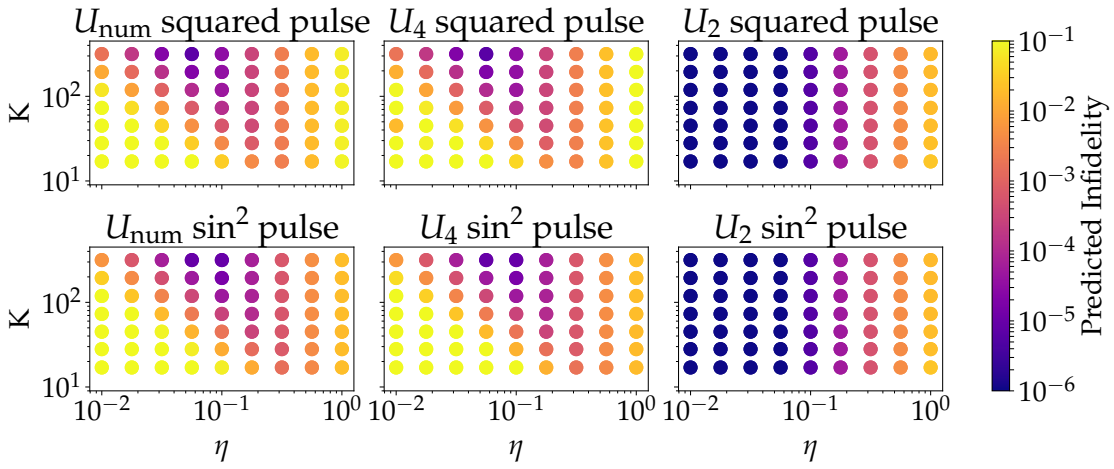

Figure B.1.: Predicted infidelity (color-coded) as a function of η and K. The fixed parameters are $K - L = \frac{\nu-\delta}{2\pi}T = 3$, $\nu/(2\pi) = 1\,\text{MHz}$, $\bar{n} = 2 \times 10^{-2}$, and $\Omega = \Omega_2$, defined in Eq. (2.70). Top: results for squared pulses Bottom: results for a sin^2-shaped drive. From left to right, the results for simulation using the Trotter propagator $\hat{U}_{\text{num}}$, the propagator $\hat{U}_4$, and the propagator $\hat{U}_2$ are shown.